

High-temperature photovoltaics for Solar Electric Propulsion Oberth Maneuver: ton-class payload feasibility for 200 AU interstellar-precursor missions

Nadim Maraqtan^{a,e,*}, Willem van Lynden^b, Carlos Gómez de Olea Ballester^{c,e}, Andreas M. Hein^{d,e}

^a*University of Stuttgart, Institute of Space Systems, Pfaffenwaldring 29, Stuttgart, 70569, Germany*

^b*Aliena Pte Ltd, 6 Ubi View, Singapore, 408544, Singapore*

^c*Technical University of Munich, Arcisstraße 21, Munich, 80333, Germany*

^d*University of Luxembourg, Interdisciplinary Centre for Security, Reliability and Trust (SnT), Luxembourg, L-1359, Luxembourg*

^e*Initiative for Interstellar Studies, 2729 South Lambeth Road, London, SW8 1SZ, UK*

Abstract

In-situ exploration beyond the giant planets remains rare, limited by the energy required for solar system escape. Motivated by laboratory demonstrations of high-intensity, high-temperature (HIHT) solar cells with demonstrated operation at 400 °C, we assess a Solar Electric Oberth Maneuver with perihelion 0.3 AU. For a Falcon Heavy launch, evolutionary steering optimization indicates that delivering 1,000-kg-class scientific payloads to 200 AU within 25 years is feasible if HIHT electrical power systems achieve specific powers about 10% above present-day levels of conventional systems when utilizing a Jupiter gravity assist, or about 2× present-day levels for a direct trajectory. The performance gain is explained by more efficient specific-energy transfer: the near-Sun maneuver yields a threefold specific orbital energy increase compared with a 1 AU outward spiral at the same Δv , defining an architectural feasibility envelope for ton-class heliopause missions without nuclear propulsion or costly SLS-class launchers under the stated assumptions.

Keywords: Solar Electric Propulsion, Solar Oberth Maneuver, High-Temperature Solar Cells, Evolutionary Neurocontrol, Interstellar Precursor

1. Introduction

Despite decades of near-Earth exploration, the outer heliosphere and heliopause remain sparsely sampled by in-situ missions, limiting our understanding of large-scale heliospheric structure, solar-interstellar coupling, and outer-heliosphere particle populations. Only a small number of spacecraft have achieved the high-energy solar system escape trajectories required for timely in-situ measurements in these regions. This leaves key aspects of the heliosphere–interstellar-medium interaction at heliocentric distances on the order of 200 AU largely uncharacterized [1, 2, 3, 4]. Addressing this gap is a major scientific and exploration goal which requires mission architectures that deliver high solar system escape energy while retaining meaningful payload capability.

This limited sampling is primarily driven by the mismatch between the specific orbital energy required for timely solar system escape and the practical limits of current propulsion systems. These constraints restrict both achievable payload mass and overall mission duration. We therefore optimize allocatable science payload mass m_{pl} , interpreted here as the instrument suite and payload-specific hardware. Payload capability is treated as margin in sensitivity trades against EPS specific power and spacecraft structural-mass-fraction assumptions.

Conventional chemical propulsion, while robust and well understood, provides limited payload capacity and typically requires costly super-heavy-lift launchers. For example, published estimates place SLS Block 1B production cost at \$2.5 billion (excluding systems engineering and integration) [5], whereas commercial heavy-lift procurement is reported at the order of \$0.15 billion for selected missions [6]. Moreover, multiple stages or complex gravity-assist sequences are commonly required to reach the high heliocentric velocities needed for deep-space exploration [7]. The Voyager missions, for example, have provided key scientific insights beyond 130 AU [8, 9, 10, 11], but their trajectories relied on the rare “Grand Tour” alignment of the outer planets [12] that occurs only every ~175 years [13]. Even with this favourable geometry, both spacecraft are now limited by asymptotic speeds of less than 4 AU year⁻¹ and aging systems, restricting further in-situ exploration.

These limitations motivate architectures that increase delivered specific orbital energy without relying on new propulsion physics. Here we examine a Solar Oberth Maneuver (SOM) enabled by high-power Electric Propulsion and laboratory-demonstrated high-intensity, high-temperature (HIHT) photovoltaics. Executing Δv near perihelion increases the gain in delivered specific orbital energy per unit Δv . Prior solar Oberth studies largely rely on impulsive chemical or solar-thermal stages with heavy thermal protection [7, 14] or on high-performance solar sails [15], leading either to high parasitic

*Corresponding author.

Email address: nadim.maraqtan [at] irts.uni-stuttgart.de
(Nadim Maraqtan)

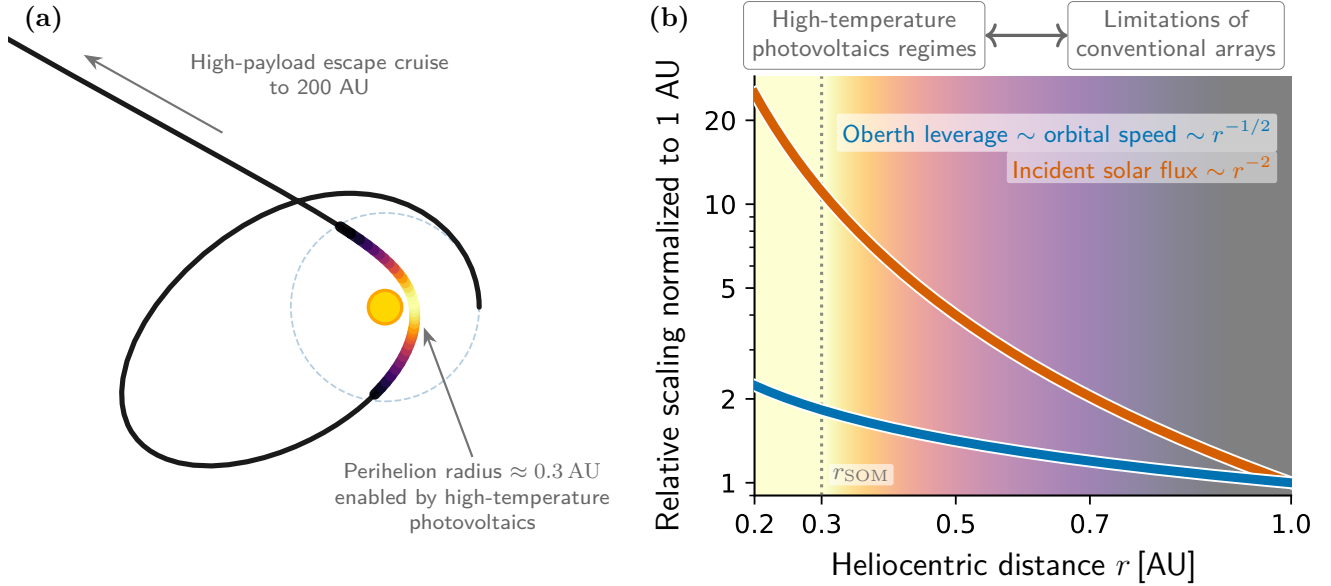


Figure 1: Solar Electric Propulsion - Solar Oberth Maneuver concept and near-Sun scaling. (a) Schematic of the SEP-SOM architecture, in which Solar Electric Propulsion delivers the spacecraft to a low perihelion and thrust is applied near perihelion to increase delivered specific orbital energy, enabling a high-payload escape cruise to ~ 200 AU. (b) Relative scaling with heliocentric distance r , normalized to unity at 1 AU, of perihelion orbital-speed leverage ($\propto r^{-1/2}$) and incident solar flux ($\propto r^{-2}$). The vertical marker indicates the reference perihelion radius $r_{\text{SOM}} \approx 0.3$ AU considered in this study.

mass / launch demands or to kilogram-scale payloads. Existing solar Oberth concepts (see Table 1) have not demonstrated ton-class payload delivery to ~ 200 AU within 25 years under non-nuclear propulsion assumptions and commercial launch mass limits, motivating a solar electric variant.

Electric Propulsion (EP) offers high I_{sp} and efficient propellant use [16]. In principle, the steep rise in solar irradiance toward perihelion can increase available power, making SEP-SOM attractive for outer-solar system and interstellar-precursor missions [17, 18]. However, prior solar electric Oberth concepts [19] have been strongly constrained by thermal limits of conventional (non-HIHT) solar cells. To avoid cell degradation, these studies typically impose conservative minimum perihelia of $r_{\text{SOM}} \approx 0.5\text{--}0.7$ AU [7, 19, 20], where both perihelion velocity and irradiance are only modestly increased, yielding a correspondingly muted Oberth contribution and power level of only a few solar constants. Consequently, these thermally constrained architectures typically yield payloads of only tens to a few hundred kilograms to heliopause-like distances. This bottleneck is best seen by contrasting the near-Sun scalings of orbital-speed leverage and available solar power, alongside the SEP-SOM architecture (Fig. 1).

Recent advances in HIHT solar cell technology suggest a route to relaxing this bottleneck. Laboratory work by Perl *et al.* [21, 22] and related studies [23] have demonstrated that modern multi-junction cells can sustain efficient operation at temperatures approaching 400°C under concentrated illumination in laboratory conditions. Building on these results, this study assumes HIHT survivability at $T \approx 400^{\circ}\text{C}$ for the reference near-Sun operating condition and varies EPS specific power in

the sensitivity analysis. For the reference trajectory optimization, a system-level EPS specific power of $\alpha_{\text{EPS}} = 200 \text{ W kg}^{-1}$ at 1 AU (including power processing units, PPU) is used as an illustrative high-performance anchor, aligned with published development targets for non-HIHT solar electric power subsystems (see Section 2.3). This baseline is used to quantify architectural leverage, not as a required feasibility threshold or near-term forecast; Section 5.4 then maps payload feasibility across lower and intermediate α_{EPS} values.

Given these technology assumptions, the present work provides an architecture-level assessment of a high-payload SEP-SOM architecture at $r_{\text{SOM}} \approx 0.3$ AU, enabled by HIHT solar arrays. We quantify the delivery of ton-class payloads to the heliopause (~ 200 AU) within 25 years using an expendable Falcon Heavy launch as an alternative to SLS-class heavy-lift options. This article extends a preliminary architectural assessment [24]. It fully documents the optimization framework including verification and validation, expands the sensitivity analysis via scaling relations and parameter maps, and adds trades against nuclear electric and impulsive Oberth concepts. This contextualizes related analytic perihelion estimates for advanced SEP probes [17].

To make the feasibility case transparent and reusable, we outline five main contributions: (i) an architecture-level SEP-SOM baseline at $r_{\text{SOM}} \approx 0.3$ AU that quantifies payload delivery under lumped subsystem assumptions and evaluates Falcon Heavy feasibility; (ii) a synthesis of prior solar Oberth concepts and near-Sun power constraints, distilling design drivers for low-perihelion SEP-SOM; (iii) the introduction, verification and benchmark validation of the SOMBRERO (Solar Oberth Ma-

neuver By Realization of EvolutionaRy Algorithm) evolutionary optimization framework for planar SEP–SOM steering; (iv) the derivation and application of generalized payload-scaling relations and sensitivity maps for key parameters (EPS specific power and structural mass ratio); and (v) an interpretation of results positioning the HIHT-enabled SEP–SOM as a high-payload solar-escape architecture, contrasted with impulsive Oberth and nuclear electric approaches.

2. Background and Literature Review

This section summarizes prior SOM studies using diverse propulsion concepts. Moreover, we discuss recent advances in high-temperature solar cells, and the engineering and TRL gaps that must be closed to mature them into a flight-qualified, lightweight panel.

2.1. Solar Oberth Maneuver Theory

Let ε denote heliocentric specific orbital energy, $\Delta\varepsilon$ its change due to propulsion, r the heliocentric distance, Δv a propulsive velocity increment, and I_{sp} the specific impulse. Let $\mathbf{v}(t)$ be the heliocentric velocity and $v(t) = \|\mathbf{v}(t)\|$ its magnitude; a denotes the heliocentric semi-major axis and r_p the perihelion radius. Maximizing the Sun–escape speed is equivalent to maximizing ε . Because the onboard Δv is limited, it is useful to maximize $\Delta\varepsilon$ per unit Δv . The Oberth effect states that a prograde burn yields a larger $\Delta\varepsilon$ when executed at high v (deep in the potential well, i.e., small r); for the Sun this is termed a Solar Oberth Maneuver (SOM) [25].

In the impulsive limit, a prograde Δv changes specific orbital energy by $\Delta\varepsilon = v\Delta v + \frac{1}{2}(\Delta v)^2$, highlighting why applying Δv near perihelion (high v) is advantageous. In practice, chemical stages can concentrate Δv near perihelion but are typically constrained in total Δv by I_{sp} .

Electric Propulsion systems, on the other hand, implement Δv over finite time, so an integral form needs to be considered:

$$\Delta\varepsilon = \int_{t_0}^{t_f} \mathbf{v}(t) \cdot \mathbf{a}_T(t) dt = \int_{t_0}^{t_f} v(t) \frac{F_T(t)}{m_{sc}(t)} \cos\theta_T(t) dt, \quad (1)$$

where $[t_0, t_f]$ is the thrust arc, $v(t)$ is the orbital speed, $F_T(t)$ is the thrust magnitude, $m_{sc}(t)$ is the instantaneous spacecraft mass, and $\theta_T(t)$ is the angle between the thrust and velocity vectors. The integrand $v(t)F_T(t)/m_{sc}(t) \cos\theta_T(t)$ is the specific mechanical power delivered by propulsion; maximizing its time integral maximizes $\Delta\varepsilon$.

For an EP–SOM, a lower perihelion is attractive because it increases (i) the local orbital speed and thus the energy leverage per unit Δv , and (ii) the available solar electric power (and hence attainable thrust acceleration) at small r , allowing more of the thrust work to be delivered during the high- v perihelion arc. For illustration, for $a = 3$ AU, reducing r_p from 0.7 to 0.3 AU increases perihelion speed from ≈ 47.4 to 75.0 km s $^{-1}$ (+58%). Together, lower perihelion increases both the speed $v(t)$ and the attainable thrust acceleration component along the velocity, $a_{||}(t) \equiv F_T(t)/m_{sc}(t) \cos\theta_T(t)$, thereby increasing the integrand in (1) and motivating thrust work concentrated near perihelion.

2.2. Solar Oberth Maneuver Literature Review

Prior Solar Oberth Maneuver studies span impulsive staging, sail-based concepts, and solar electric architectures. Across these proposals, high escape energy is typically traded for parasitic mass, conservative perihelia, or both, which limits delivered science capability in the reported reference cases. Table 1 summarizes representative studies and reproduces payload figures as stated in the cited sources, with the payload definition indicated in the table caption. The proposals generally fall into three distinct categories:

1. High-Thrust Impulsive SOMs: This category, which includes Chemical Propulsion, Solar Thermal Propulsion (STP), and Nuclear Thermal Propulsion (NTP), seeks to maximize the Oberth effect by adopting extreme-proximity perihelia, typically ranging from 2–11 solar radii (R_\odot) [7, 14, 26]. The resulting thermal environment necessitates massive, robust thermal-protection systems (TPS). The parasitic mass of this heat shield and/or active cooling hardware curtails the available *science payload* or residual payload margin, with reported science payloads in the tens-of-kilograms range in some studies [27] and emphasizing tight residual-mass margins once staging and any required perihelion heat shielding are accounted for [28]. Furthermore, these architectures often depend on high-cost, heavy-lift launchers such as the SLS to provide the requisite launch energy [7, 14, 29]. At the trajectory level, such low-perihelion, high-thrust SOMs are highly sensitive to injection and navigation errors: once the impulsive burn has been executed, any mismatch between the targeted and achieved perihelion state rapidly maps into large errors in the outgoing hyperbola, leaving little scope for post-SOM correction. When these impulsive SOMs are embedded in additional gravity-assist sequences (e.g. JGA), the overall mission-design and operations complexity, as well as sensitivity to launch-window phasing, increases significantly.

2. High-Performance Solar Sails: While capable of achieving very high escape velocities ($20 - 60$ AU year $^{-1}$) by harnessing solar radiation pressure at close perihelia (2–5 R_\odot), solar sails are fundamentally mass-limited. Their performance is dictated by an extreme area-to-mass ratio and very large deployable structures, which typically restricts the delivered dry spacecraft mass to the kilogram-to-tens-of-kilograms class [15, 30, 31].

3. Thermally constrained Solar Electric SOMs (high-perihelion): This category, the most relevant to the present study, has historically been power-system-constrained [32]. To protect conventional solar arrays from thermal damage, prior Solar Electric SOM studies, including work explicitly framed as a “Solar Electric Oberth Manoeuvre” [19], are confined to conservative perihelia of $r_{SOM} \approx 0.5\text{--}0.7$ AU [19, 20, 32]. This high-perihelion approach has two fundamental disadvantages:

it blunts the Oberth leverage by limiting perihelion velocity, and it restricts the available solar intensity for the electric thrusters to only $\lesssim 4$ solar constants. Consequently, these thermally constrained concepts yield comparatively low *science payloads* where reported (e.g., 35–150 kg instrument mass) and do not provide a viable pathway to high-payload missions [20, 32, 33].

Taken together, the literature does not yet establish a SOM architecture that supports a large allocatable mission payload: impulsive concepts are limited by parasitic thermal-protection mass, while prior solar electric concepts are limited by thermally constrained, high-perihelion trajectories. Table 1 provides a quantitative summary of key assumptions, performance parameters, and limiting factors. For completeness, non-electric SOM implementations (chemical, solar sail, solar thermal, and nuclear thermal) are reviewed in Appendix A. The remainder of this subsection focuses on electric-propulsion SOM architectures (Section 2.2.1), which form the closest antecedent to the present feasibility model.

2.2.1. Electric Propulsion SOM

Literature on Electric Propulsion (EP) Solar Oberth Maneuvers is limited, mainly due to thermal constraints on conventional solar arrays. Identified studies have been summarized in Table 1.

Kluever [32] analysed a SEP mission to 200 AU using a Titan IV/Centaur launch, carrying a 150 kg scientific payload, constrained to a 0.7 AU perihelion to protect solar cells, which could reach 200 AU in 18–20 years. More recently, Loeb and Ohndorf [20, 33] proposed a smaller Ariane 5-launched mission (1,692 kg) requiring a JGA and Radioisotope Electric Propulsion (REP) stage to reach 200 AU in 25 years, leaving only 35 kg for scientific payload. This apparent decrease in performance compared to the Kluever study is attributable to the significantly different initial mission constraints, particularly the $\sim 77\%$ smaller launch mass. Their proposal serves as reference for the paper at hand, as the developed neurocontrol algorithm is verified using their results. Finally, Bering et al. [19] investigate solar and hybrid EP mission concepts to the Kuiper Belt and beyond, including a trajectory with Saturn and Neptune gravity assists, where the Neptune flyby serves as a gravity assist for an Eris flyby and subsequent coast to 1,000 AU in 125 years, corresponding to an average of 8 AU year $^{-1}$. The concept places perihelion near 0.5 AU, and one illustrated case shows a closest solar approach of 0.657 AU. Their ice-giant modeling builds on a stated propulsion basis model that assumes argon operation with $I_{sp} \approx 5,200$ s out to 1 AU outbound, followed by a switch to hydrogen with assumed $I_{sp} = 32,800$ s. A refined variant includes jettison of depleted argon tankage near 1 AU and assumes a spacecraft launch mass of roughly 30 t and an Earth-relative hyperbolic excess speed of $v_{\infty,Earth} \approx 5$ km s $^{-1}$, implying $C_3 \approx 25$ km 2 s $^{-2}$. For the 1,000 AU case, delivered payload mass and EPS or array specific-power assumptions are not reported alongside the time-of-flight result.

While literature explicitly framing a low-perihelion, solar-powered EP thrust arc as an Oberth-type maneuver for solar

system escape remains limited, conceptually adjacent strategies appear in the broader SEP mission literature for high-energy interplanetary transfers. These related concepts generally remain in a more conservative near-Sun regime and rely on explicit array thermal control. Zola [39] presents early SEP probe concepts and shows a representative array power profile that is flattened below about 0.65 AU by tipping the panel to maintain roughly constant equilibrium temperature. Rodgers and Brophy [40] propose the TEMPO concept for a fast Pluto flyby and note that the array is feathered for thermal control below 1 AU, with temperature margin down to about 0.6 AU. Ilin et al. [41] survey VASIMR mission strategies and include a reusable catapult concept that uses an inward arc to raise solar power and then accelerates near the Sun. Their example reaches $R_{min} = 0.452$ AU and assumes planar arrays to avoid overheating photovoltaic cells. These studies are not treated as SEP–SOM escape analyses and are therefore not included in Table 1. They support the broader idea that near-Sun Solar Electric Propulsion can front-load energy for fast outer-planet transfers and other high-energy missions. They also help delineate the remaining gap addressed here, namely that pushing solar-powered EP thrusting to substantially smaller perihelia requires higher-temperature EPS and array capability.

2.3. Electric Power System Literature Review

The minimum perihelion for a SOM is primarily limited by thermal constraints. Close to the Sun, temperatures and high-intensity solar irradiation can severely degrade solar cell performance [42, 17], while the spacecraft structure itself must also withstand extreme heating. Thermal shielding can protect the spacecraft, but the solar panels must remain exposed to collect power for the propulsion system, making HIHT solar cells a critical enabling technology.

Only a few missions have flown close to the Sun. Helios 1 and 2 (1974–1976) reached 0.29 AU using silicon cells on angled panels with quartz mirrors and partial active cooling to limit temperatures to $\sim 160^\circ\text{C}$ [43]. Parker Solar Probe (2018) reached 0.044 AU, using advanced multi-junction cells, which are designed for $\sim 125^\circ\text{C}$ and required active cooling behind the heat shield to survive Sun-facing temperatures up to $\sim 1370^\circ\text{C}$ [44, 45]. The Solar Orbiter (2020) reaches 0.28 AU with triple-junction GaAs cells capable of $\sim 230^\circ\text{C}$, supplemented by reflective coatings and panel tilting to limit solar absorption [46, 47, 48]. Mercury orbiters such as Messenger and BepiColombo, as well as earlier Venus and Mercury missions like Mariner 10 and the Venera series, also faced near-Sun conditions requiring similar strategies.

These missions employ four main approaches to ensure solar panel survival: (i) using specialized high-temperature cells, (ii) reducing incident solar irradiation through tilting or shading, (iii) lowering panel absorption via reflective coatings or mirrors, and/or (iv) including active cooling. Active cooling adds mass, reducing payload, while shading or reflective coatings limit the power collected. To maximize power during a SOM and exploit the Oberth effect, it is therefore critical to capture as much solar flux as possible, highlighting HIHT solar cells as a central enabling technology. Notably, the present

Table 1: Solar Oberth Maneuver mission metrics reported in the literature for benchmarking. Payload-mass definitions are indicated by superscripts.

Prop. Type	Reference	Launcher Type	C_3 [km ² s ⁻²]	r _{SOM} [AU]	m ₀ [kg]	m _{pl} [kg] [†]	v _{∞,∞} [AU year ⁻¹]	t _{200AU} [yr]	Performance / Key Limitation
Chemical	Hopkins et al. [7]	SLS 1B + JGA	≈ 135	≈ 0.05 ^c	(N/A)	~ 380 ^{Da}	≈ 10	≈ 20	100+ AU in 10 yrs
Chemical	Hibberd et al. [29]	SLS B2 + JGA	≈ 100	(low)	(N/A)	100 ^D	≈ 8.5	≈ 24	Chem. stages only for SOM; otherwise SEP / Solar Sail
Chemical	Hibberd & Eubanks [34]	Starship B3 + JGA	≈ 130	≈ 0.015	16,450 -17,754	342- 546 ^D	≈ 10–20	≈ 13	~47 yrs to 400 AU. General feasibility study. Heat shield mass not accounted for.
Solar Sail	Davoyan et al. [15]	(N/A)	(N/A)	0.05	(N/A)	10–50 ^D	> 20	< 10	Requires > 10,000 m ² sail.
Solar Sail	Liewer et al. [35]	Delta II	(N/A)	≈ 0.25	≈ 246	25 ^I	≈ 15	≈ 15	400 m sail (~ 1 g m ⁻²).
Solar Sail	Bailer-Jones [30]	(N/A)	(N/A)	0.05–0.53	(N/A)	(N/A) ^U	(N/A)	(N/A)	Theoretical trajectory study; analyzes maneuver efficiency.
Solar Sail	Davoyan et al. [31]	(N/A)	(N/A)	< 0.023 ^c	10–20	12–16 ^D	≈ 60	≈ 3	~1,000 AU in ≈ 17 yrs (concept).
Laser Sail	Hibberd et al. [36]	(N/A)	(N/A)	≈ 0.015 ^c	< 1	< 1 ^D	≈ 63.2 ^b	≈ 3	Gram–kg class (0.001c).
STP	Shoji et al. [37]	(N/A)	(N/A)	≈ 0.02 ^c	(N/A)	(N/A) ^U	≈ 11.0	≈ 18	Early conceptual study.
STP	Lyman et al. [26]	JGA	(N/A)	≈ 0.016 ^c	~ 50	~ 50 ^D	20.0	10	Limited by heat shield.
STP	Sauder et al. [27]	SLS B2 + GA ^d	(N/A)	≈ 0.015 ^c	478	36 ^I	8.0–10.0	≈ 20–25	Various gravity assists.
STP	Benkoski et al. [14]	SLS + JGA	165	≈ 0.01 ^c	5,000	661.6 ^D	15.0	≈ 13	Limited payload.
NTP	Hibberd & Hein [28]	SLS	(N/A)	(low)	1,300 - 7,800	(limited) ^U	(N/A)	(N/A)	Residual mass margin highly limited.
NTP	Irvine et al. [38]	SLS	(N/A)	≈ 0.05 ^c	(N/A)	(constr.) ^U	≈ 15.6	≈ 13	500 AU in ≈ 32 yrs.
EP	Kluever [32]	Titan IV	(N/A)	0.7	7,500	150 ^I	10.0–11.1	≈ 18–20	Thermally limited.
EP	Loeb et al. [33]	Ariane 5 + JGA	45.1	0.7	1,692	35 ^I	8.0	25	Thermally limited. REP ^e stage required.
EP	Ohndorf et al. [20]	Heavy Lift + SGA + NGA ^f	25	0.5–0.66	30,000	(N/A) ^U	8.0	25	1,000 AU in 125 yrs; thermally limited.

[†]Payload values are reproduced as stated in the cited sources; superscripts indicate the payload definition.

^IScience payload (instrument mass) as defined in the cited source.

^DDelivered dry spacecraft mass, excluding propellant and any jettisoned transfer/propulsion stage, as defined in the cited source.

^UPayload definition not specified or ambiguous in the cited source (or no mission payload value reported).

^aBaseline bus ~380 kg; additional ~300 kg heat shield required.

^bFrom 0.001c; 1c ≈ 63,241 AU year⁻¹.

^cConverted from value in R_\odot ; $R_\odot \approx 0.00465$ AU.

^dEGA (Earth Gravity Assist) + VGA (Venus Gravity Assist) + JGA (Jupiter Gravity Assist)

^eRadioisotope Electric Propulsion

^fSGA (Saturn Gravity Assist) + NGA (Neptune Gravity Assist)

lumped-parameter mass budget omits a separate Parker Solar Probe–style dedicated heat shield and active-cooling hardware for the spacecraft bus. Instead, the bus is assumed to remain largely in the geometric shadow of the Sun-facing HIHT arrays during the perihelion arc; any residual shielding or thermal-control mass is subsumed into the structural mass fraction μ_s and not modeled explicitly.

2.3.1. Advancements in High-Temperature Solar Cells

HIHT solar cells have been studied for decades, motivated by missions to Mercury, Venus, and near-Sun exploration. The

BepiColombo solar arrays provide a recent flight-demonstrated example, employing GaAs triple-junction cells (AZUR 3G28) which are however only validated for operational temperatures up to 215°C [57]. Similarly, Parker Solar Probe utilizes triple-junction cells, but relies on active cooling to maintain operating temperatures near 160°C [58]. While these missions represent the current state of flight-ready technology, research shows that laboratory and near-Sun designs can operate at far higher temperatures without such extensive thermal control. Table 2 presents a compilation of recent developments, highlighting the

Table 2: Summary of High-Intensity High-Temperature (HIHT) solar cell developments. Reported temperatures refer to cell-level results. Array-level integration and system-level power-processing impacts are treated separately.

Material / Cell Type	Sustained / Tested Temperature	Intended Application	Reference(s)
GaInP	~ 400°C (predicted)	Early HIHT concept for Mercury-, Venus-, and near-Sun exploration.	[49]
GaAs/AlGaAs concentrator cells	> 500°C (survived to 800°C)	High-intensity concentrator photovoltaics subjected to extreme thermal cycling.	[50]
SiC (6H-SiC) solar cells	Up to 600°C	Operation within ~3 solar radii (≈ 0.014 AU); very high-temperature near-Sun missions.	[51]
InGaP/InGaAs/Ge triple-junction	Up to ~ 240°C	Cells designed for near-Sun operation and high-flux illumination (~1,000× concentration).	[52]
InGaP/GaAs/Ge triple-junction	Up to ~ 240°C	Near-Sun missions; similar architecture to [52] with thermal optimisation.	[53]
AlGaInP, GaAs, GaInP/GaAs dual-junction	Up to 400°C	HIHT laboratory cells approaching near-Sun operational requirements (up to ~345× solar flux).	[54, 21, 22]
GaInP/GaAs (Venus-lander design)	Up to 465°C	Photovoltaic systems tailored for Venus's extreme surface temperature environment.	[55]
InGaN-based HIHT cells	Up to 450°C	Next-generation HIHT photovoltaics for extreme-temperature space environments.	[56]

progression of HIHT photovoltaics toward practical near-Sun applications at temperatures exceeding 400 °C.

These results are largely cell-level. Further development into full, flight-like panels with appropriate component shielding [59], combined with strategies like sun-screen filtering, could allow full solar exposure at perihelion, maximizing power capture without relying on tilting [47, 59] or active cooling.

2.3.2. Specific power

Beyond surviving the near-Sun environment, an equally important metric for solar-driven Electric Propulsion missions is the specific power α —the power delivered per unit mass. For the majority of commercially developed triple-junction cells, $\alpha_{\text{cell}} < 800 \text{ W kg}^{-1}$, with efficiencies in the range of 20-30% [60, 61].

Significant progress has been made in further increasing cell-level α . Commercial Off-The-Shelf (COTS) triple-junction cells have been commercially developed with specific powers up to 3,200 W kg^{-1} [61] while many other advanced multi-junction and perovskite cells have achieved specific powers above 1,000 W kg^{-1} [62, 63, 64], with some exceeding 10,000 W kg^{-1} [65, 66].

Array assembly components beyond the solar cells (cover glass, structure, insulation, harness) reduce the array-level specific power α_{array} relative to α_{cell} ; thermal-mitigation strategies (tilting, reflective optics, active cooling) can further reduce α_{array} . If the solar array provides α_{array} and the power-processing unit (PPU) provides α_{PPU} , the combined EPS performance is given by

$$\alpha_{\text{EPS}} = (1/\alpha_{\text{array}} + 1/\alpha_{\text{PPU}})^{-1}. \quad (2)$$

Recent surveys of deployable arrays report array-level specific powers exceeding 100 W kg^{-1} (e.g., iROSA) and $\sim 112 \text{ W kg}^{-1}$

for the Phoenix UltraFlex wing (flight heritage). These configurations both could potentially provide even higher specific powers, $\sim 218 \text{ W kg}^{-1}$ and $\sim 250 \text{ W kg}^{-1}$ respectively [61]. Assuming comparable scaling, Perovskite panels might reach a tenfold increase, reaching $\gtrsim 2,000 \text{ W kg}^{-1}$. While further research is required to validate these projections and to develop heat-resistant panel structures, these advances suggest that combining HIHT capability with high- α cells may enable significantly more powerful Electric Propulsion systems operating much closer to the Sun than is currently feasible.

Present-day PPUs report $\alpha_{\text{PPU}} = 266 \text{ W kg}^{-1}$ [67] (Lunar Gateway). Together with $\alpha_{\text{array}} = 112 \text{ W kg}^{-1}$, Eq. (2) yields $\alpha_{\text{EPS}} \approx 78.8 \text{ W kg}^{-1}$ as an order of magnitude value for present-day solar electric EPS-level specific powers.

Beyond heritage hardware, multiple agency studies cite a development objective of 200 W kg^{-1} for deployable solar-array specific power α_{array} . The ESA High-Efficiency Solar Arrays study targets 200 W kg^{-1} for concepts above 150 kW [68]. A NASA program description for MegaFlex cites a wing-level goal of 200 W kg^{-1} at the beginning of mission near one astronomical unit [69]. Propulsion reviews discuss similar spacecraft-level projections over five to ten years [70]. At system level the electrical power subsystem specific power α_{EPS} remains below α_{array} unless the power processing unit, PPU, improves comparably. Using the present-day example above, $\alpha_{\text{EPS}} = 200 \text{ W kg}^{-1}$ under uniform scaling implies $\alpha_{\text{array}} \approx 280 \text{ W kg}^{-1}$ and $\alpha_{\text{PPU}} \approx 665 \text{ W kg}^{-1}$. The implied PPU value should be read as a stretch target, not a heritage-level value. For context, NASA GRC projected an optimized 14 kW-class Hall-thruster PPU at $\gtrsim 330 \text{ W kg}^{-1}$ [71], while SiC-based developments target $> 2500 \text{ W kg}^{-1}$ at converter-stage level [72].

2.4. High Power Electric Propulsion Literature Review

For the reference mission, an electric thruster with $I_{sp} = 6,000$ s and $\eta = 0.75$ is assumed. Such values are achievable with several thrusters with varying stages of technology readiness, such as gridded ion thrusters (GIT) [73, 74, 75] and applied-field magnetoplasmadynamic thrusters (AF-MPD) [76, 77]. Thrusters identified to meet or nearly meet the reference mission required values are listed in Table 3.

GITs offer substantial flight heritage and remain the most mature route to high- I_{sp} operation at high efficiency. AF-MPD thrusters are at lower TRL and lack flight demonstration. However, the laboratory results in Table 3 approach the reference operating point. If this performance can be sustained with demonstrated lifetime and system-level integration, AF-MPD concepts are credible candidates for higher-power stages, offering high thrust density, compact packaging, and good throttling capability. Accordingly, flight-proven GITs serve as the conservative baseline, while AF-MPDs offer a high thrust-density alternative to mitigate the clustering complexity inherent to megawatt-class architectures. In the present model, the EP system is represented as an aggregated thruster cluster with constant I_{sp} and η .

3. Reference Mission Definition

Building on the preceding review and the HIHT photovoltaic assumptions, we define a reference SEP–SOM mission to quantify delivered payload mass at 200 AU within 25 years.

This objective is aligned with outer-heliosphere concepts such as NASA’s Interstellar Probe concept [1, 91], which target heliopause-class distances on multidecadal timescales with a substantial payload to characterize heliospheric structure and its interaction with the very local interstellar medium, including energetic particles, dust, fields, and interstellar plasma. Representative payload elements include plasma and energetic neutral atom sensors, magnetometers, cosmic-ray and dust analyzers, UV/visible imagers, and radio and plasma-wave instruments.

While trajectory concepts optimized for ultra-light payload masses could in principle reach 200 AU in shorter times, the present study adopts a different figure of merit: for a fixed target distance and transfer time, we maximize delivered payload mass. In the adopted lumped-parameter spacecraft model, payload mass is the adjustable part of the dry-mass budget and therefore directly measures allocatable science capability and margin. This choice also supports the sensitivity analysis: it makes the dependence on the enabling parameter α_{EPS} explicit, with additional sensitivity to the lumped structural/bus mass fraction μ_s , quantified in Section 5.4. This facilitates the derivation of the minimum viable α_{EPS} for the maneuver to become implementable.

The mission comprises launch, a SEP spiral that raises aphelion and lowers perihelion to r_{SOM} , the near-perihelion SEP–SOM thrust arc, an optional Jupiter transfer and gravity assist, and a ballistic cruise to 200 AU. Beyond Jupiter orbit, the propulsion system is inactive. The quantitative reference-case

choices (baseline r_{SOM} , launcher interface, and whether a JGA is used) are collected in Section 4.2.

4. Methodology

Identifying an effective steering strategy for a low-thrust mission is challenging, since at every time step it must be decided whether to thrust, with which magnitude, and in which direction. Classical low-thrust trajectory optimisation is typically addressed with indirect optimal-control methods based on Pontryagin’s Maximum Principle or with direct transcription and collocation schemes that discretise the trajectory and solve the resulting nonlinear programme. These approaches often rely on adequate initial guesses and expert knowledge in astrodynamics and control theory [92, 93], and the obtained solutions tend to remain in the vicinity of the initial guess, which does not necessarily coincide with the (unknown) global optimum [94].

Dachwald introduced evolutionary neurocontrol (ENC), in which an evolutionary algorithm optimizes the weights of a neural-network controller that maps spacecraft state variables to thrust commands [95]. The InTrance framework developed by Dachwald and later extended by Ohndorf is the most widely used ENC implementation for low-thrust trajectory design [95, 93] and can employ up to 28 spacecraft state inputs for fully three-dimensional, multi-phase problems. Motivated by the planar SEP–SOM setting and the need for lower-dimensional inputs and simplified evolutionary operators [93], we developed the SOMBRERO algorithm in Python. SOMBRERO implements a planar evolutionary neurocontroller with only four spacecraft state inputs and uses a mutation-based evolutionary operator. This approach avoids the need for carefully crafted initial guesses and provides a global search mechanism suitable for the strongly non-linear, non-convex SEP–SOM design space.

In the following, we define the spacecraft model, scope and validity bounds as well as the numerical trajectory integration setup, and the details of the evolutionary scheme used in SOMBRERO.

4.1. Spacecraft Model

This study is a conceptual mission-architecture assessment for a Solar Electric Propulsion Oberth Maneuver with small perihelia, rather than a fully detailed mission design. Accordingly, a simplified spacecraft model is employed and explicit mass margins are not applied at this stage. The total spacecraft launch mass m_0 is assumed to be composed of four major components:

- Mission payload (allocatable dry) mass m_{pl} : mass available for the science payload and payload-specific hardware (and, equivalently, margin that may be traded into more conservative subsystem assumptions);
- Propellant mass m_p ;
- Electrical power system mass m_{EPS} (photovoltaic arrays + power processing), which determines the propulsion-relevant solar electric power via $P = m_{EPS} \alpha_{EPS}$;

Table 3: Summary of high-specific-impulse Electric Propulsion concepts and representative thruster models relevant for Solar Oberth Maneuver missions. GIT denotes a gridded ion thruster. AF-MPD denotes an applied-field magnetoplasmadynamic thruster.

Type	General Characteristics	Model	Performance Notes	I_{sp} [s]	η [-]	Power [kW]	References
GIT	<ul style="list-style-type: none"> • High I_{sp} [78] and high efficiency. • Most mature EP technology (with HET). 	NEXT-C	Flight demonstrated (DART)	4,150	0.69	-	[79]
		NEXIS	Laboratory demonstrated.	7,500–8,100	0.78–0.81	20	[80, 81]
		HiPEP	Laboratory tested.	7,500–10,000	~0.75	25	[82]
		RIT-22	Precursor RITA-10 demonstrated for ARTEMIS (2002).	3,000–6,000	> 0.8	5	[83, 84, 33]
AF-MPD	<ul style="list-style-type: none"> • High I_{sp} [85, 78], thrust density [86] and compactness • No flight heritage to date but tested in laboratory [87, 76, 88] • High-power but low TRL 	SX3	100 kW-class lab thruster	4,700	> 0.6	100	[89]
		CAST/AF-MPDT	100–150 kW class prototypes	5,600–5,714	0.76	100–150	[77, 90]

- Structure mass m_s , which comprises auxiliary subsystems (e.g., communications and attitude determination and control system) and any deep-space bus-power provision (e.g., RTG). This lumped term does not enter the solar power scaling.

For clarity, the delivered dry spacecraft mass after completion of thrusting is $m_{dry} = m_{pl} + m_s + m_{EPS}$ (excluding propellant). In this work, the optimization objective is m_{pl} . The corresponding non-dimensional mass fraction with respect to the launch mass is given by $\mu_i = m_i/m_0$. The combined mass fraction of payload and propellant at launch is $\mu_{pp,0} = \mu_{pl} + \mu_{p,0}$.

4.2. Scope, assumptions, and validity bounds

This paper is an architecture-level feasibility analysis. To avoid repeating caveats across sections, the reference-case inputs and the main validity bounds of the model are summarized here. Sensitivity to key parameters is quantified in Section 5.4.

4.2.1. Reference-case definition

The reference case is defined by the following inputs:

- *Perihelion distance:* The baseline architecture assumes a single SEP-SOM at $r_{SOM} = 0.3$ AU. This choice is motivated by the radiative-equilibrium scaling $r_{SOM} \propto T^{-2}$ for a temperature-limited array [96]. Depending on whether radiative emission is modeled from one side or from both sides of the array, this scaling implies perihelia of order 0.24–0.34 AU for $T \approx 400^\circ\text{C}$ [17] (see Appendix B.3). We use 0.3 AU as a representative central case. This Mercury-like perihelion keeps the SEP-SOM well outside the few- R_\odot regime of chemical and solar-thermal SOMs and places the spacecraft in a thermal environment comparable in order of magnitude to that encountered by Mercury orbiters such as BepiColombo.
- *Trajectory class:* Two variants are evaluated: a direct trajectory and a Jupiter-gravity-assist (JGA) trajectory. Unless noted otherwise, the JGA case serves as

the performance-oriented reference under favorable planetary phasing, and the direct case provides a window-independent alternative.

- *Launch interface:* The launch-to-escape interface is represented via a fitted injected-mass model for the fully expendable Falcon Heavy (Appendix B.5); after an exploratory phase, C_3 and launch angle are fixed to improve convergence (Validity bounds below).
- *Electrical power system:* For the reference case, a system-level value of $\alpha_{EPS} = 200 \text{ W kg}^{-1}$ at 1 AU is assumed for the overall electrical power system (including solar arrays and power-processing units), see Subsection 2.3.2; the sensitivity analysis then varies α_{EPS} to map payload-feasibility thresholds. The HIHT array structures are assumed to be operable at 400°C at the perihelion conditions of the reference SEP-SOM (see Subsection 2.3.1). These are treated as technology assumptions for the reference-case feasibility analysis (i.e., not assumed to be flight-demonstrated).
- *Available solar electric power scaling:* In the trajectory optimization, the available EPS power is modeled as $P(r) = P_{1\text{AU}}(r/1\text{AU})^{-\kappa}$ with an effective exponent $\kappa = 1.5$ (instead of the geometric inverse-square law $\kappa = 2$) to approximate temperature-related photovoltaic efficiency losses near the Sun [93, 97]. κ is used here as an effective parameter rather than a first-principles thermal model. At 0.3 AU this reduces the power increase from $(1/0.3)^2 \approx 11.1$ to $(1/0.3)^{1.5} \approx 6.1$, which deliberately avoids over-crediting near-Sun thrust authority in the Oberth-leverage regime (Subsection 2.1). This scaling should be read as a compact inner-Solar approximation of usable electrical power, not as a detailed array model across all heliocentric distances.
- *Structural mass fraction:* Following the reference heliopause-probe mass budget in [33], the structural (bus and auxiliary subsystems) launch-mass fraction is set to $\mu_s = 0.30$. In the Appendix B.6 literature-reproduction

case, $\mu_s = 0.289$. A comparable value is implied as well by the Mercury-orbiter MESSENGER dry-mass breakdown, $\mu_{s,0} \approx 0.31$ [98] (see Appendix B.2). During the near-perihelion arc, the spacecraft bus is assumed to be protected by a passive, highly reflective sunshade, as on MESSENGER [99]. There, the Sun-facing surface was predicted to reach ~ 370 °C while the bus behind the sunshade was designed to operate near room temperature (~ 20 °C) [99]. Hence, no dedicated Parker Solar Probe-style heat-shield mass (or explicit active-cooling mass) is modeled. For a MESSENGER-class mass split, the thermal subsystem fraction is below 5% of launch mass [98] and is therefore subsumed in m_s (and thus in μ_s). Sensitivity to μ_s is assessed in Section 5.4.

- *High-power Electric Propulsion:* The propulsion architecture is modeled as a modular cluster of high-power electric thrusters (e.g., AF-MPD or gridded ion units in the 50–100 kW class). To accommodate the significant variation in available solar power—ranging from ~ 330 kW at 1 AU to ~ 2 MW at 0.3 AU—the system is assumed to employ a switching strategy that activates or deactivates individual thruster strings. This operational concept allows active units to function near their nominal design points, justifying the assumption of a constant system-level specific impulse ($I_{sp} = 6,000$ s) and thrust efficiency ($\eta = 0.75$) across the broad power envelope. Detailed throttling maps, duty-cycle limits and lifetime constraints are not explicitly modeled. See the validity bounds below.

4.2.2. Validity bounds

The results should be interpreted as architecture-level performance potential rather than a fully implementable mission design. The main bounds are:

- *Technology targets:* The dominant technology uncertainty in the present study is whether high-temperature, high-specific-power solar arrays can be realized at panel and subsystem level. In the trajectory and mass model, the electrical power system is represented by a single parameter pair (T_{\max}, α_{EPS}) , with HIHT arrays parameterized by $T_{\max} = 400$ °C at perihelion and a constant reference $\alpha_{EPS} = 200 \text{ W kg}^{-1}$ at 1 AU. This abstracts away panel-level effects such as radiator and harness penalties, temporal degradation, and mechanical and thermal integration with concentration optics and the spacecraft bus. Accordingly, α_{EPS} is used here as a system-level technology target motivated by Section 2.3, not as a flight-demonstrated capability. Section 5.4 quantifies the payload penalty for lower system-level EPS specific power.
- *Spacecraft and subsystem model:* A fixed EPS specific power and structural mass fraction are assumed, together with a generic high-power EP cluster with constant I_{sp} and efficiency. Ageing, detailed thermal limits, radiation degradation and explicit mass margins are neglected, so the reported payload masses are idealized architecture-level values rather than fully margined system designs.

• *Dynamics and operations:* Trajectories are propagated in a planar, two-body (Sun–spacecraft) model, and the Jupiter gravity assist is treated analytically, and thrust is assumed to be available whenever commanded by the neurocontroller. Planetary ephemerides, out-of-plane motion, perturbations, duty-cycle limits and lifetime constraints are not explicitly modeled, which may affect achievable Δv and thrusting durations in a detailed design.

• *Optimization scope:* The evolutionary neurocontrol framework delivers high-quality, but not provably optimal, steering laws within a restricted design space.

– *Near-optimal solutions:* SOMBRERO is a stochastic optimizer with finite population. The reported trajectories should be regarded as near-optimal for the chosen setup. Additional restarts or hybrid methods could yield modest payload improvements.

– *Restricted design space:* The optimization is confined to a fixed architecture (single SOM at $r_{\text{SOM}} \approx 0.3$ AU, planar dynamics and a simplified launcher model). After an exploratory phase, C_3 and launch angle are fixed to improve convergence, excluding potentially competitive solutions with non-zero C_3 , alternative perihelia, additional assists or out-of-plane maneuvers.

– *Controller and objective:* The neurocontroller has a deliberately simple structure with a bounded thrust-angle representation and a single optimization goal (“maximize payload, provided the 25-year limit is satisfied”). This setup does not map the full trade-off between payload and flight time and may miss more complex thrusting strategies that are locally optimal within a richer control parametrization.

Thus, the reported payloads represent realistic, high-performance realizations of the proposed SEP–SOM architecture, but not strict upper bounds. More exhaustive optimization is expected to refine numerical values rather than alter the qualitative conclusions.

4.3. Evolutionary Neurocontrol Framework

We seek a steering policy $P(\chi)$ that maps the spacecraft state χ to controls \mathbf{u} and maximizes delivered payload mass m_{pl} at $R = 200$ AU under a 25-year limit, with initial conditions \mathbf{c}_0 optimized jointly. The controller genome ξ (weights and biases) is evolved together with \mathbf{c}_0 as a combined chromosome $\pi = \{\mathbf{c}_0, \xi\}$.

4.3.1. Neurocontroller

The Neurocontroller (NC) is designed to map the transformed current state of the spacecraft, represented as $\chi = \{r, v_{acc}, |\mathbf{v}|, \varphi\}$, to a steering policy $\mathbf{u} = \{\theta_T, u_P\}$, as shown in Fig. 2.

Here, the normalized heliocentric state is parameterized as:

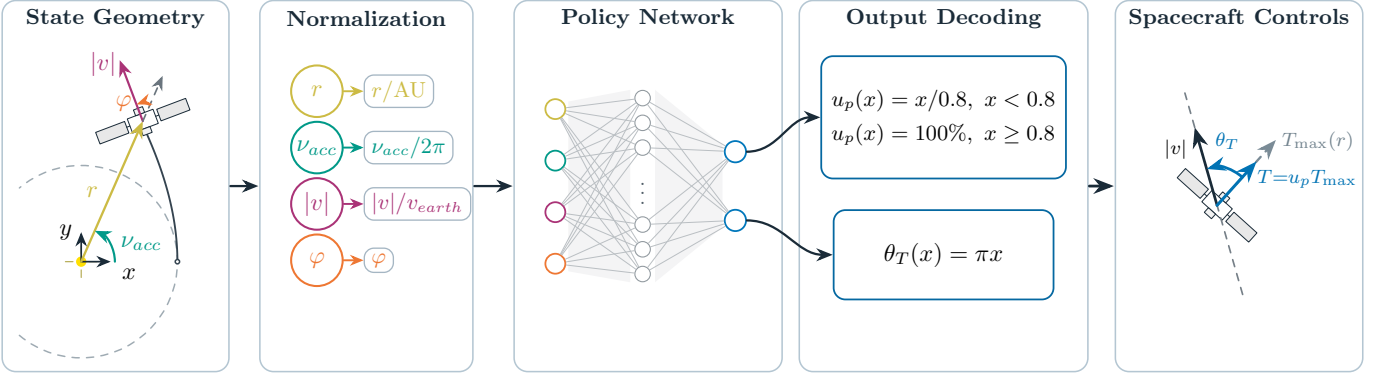


Figure 2: Evolutionary neurocontroller used in SOMBRERO. A feed-forward neural network with one hidden layer and 20 neurons maps the normalized heliocentric state $(r, \nu_{acc}, |v|, \varphi)$ to thrust angle θ_T and throttle command u_P . Weights and biases encode the steering policy and are optimized with an evolutionary algorithm.

- r is the heliocentric radial distance, normalized to astronomical units (AU),
- $\nu_{acc} = (\nu + (2\pi)_{rev>0})/2\pi$ is the accumulated true anomaly, normalized with 2π ,
- $|v|$ is the magnitude of the heliocentric velocity, normalized in units of Earth’s heliocentric velocity,
- φ is the flight path angle between the spacecraft’s velocity vector and its position vector

Together, these inputs summarize the planar heliocentric state relevant to steering. The Neurocontroller processes these inputs, all of which are normalized to the order of unity to facilitate learning. The accumulated version of the true anomaly is chosen to prevent a singularity jump from 2π to 0 close to the SOM perihelion, that otherwise obstructed the learning. Moreover, mission time information is provided this way.

The outputs of the Neurocontroller are:

- $\theta_T \in [-\pi, 0]$: the thrust angle with respect to the current direction of flight,
- $u_P \in [0, 1]$: a dimensionless throttle command scaling the electric power (realized via different mass flow rates) supplied to the thrusters, i.e. $P(t) = u_P(t) P_{max}(r(t))$. We model u_P as a continuous throttle variable representing the aggregate power fraction of a modular thruster cluster. In flight hardware, this profile would be discretized by switching individual thruster strings and modulating the duty cycle of active units.

Bounded activation functions are used to enforce physically meaningful control outputs. The exact functional forms are provided in Appendix B.1.

4.3.2. Tournament Selection

We use binary tournament selection following Dachwald [95] and Ohndorf [93]. Two individuals are drawn at random. The fitter individual is copied to the next generation. The other is replaced by crossover followed by

mutation. We employ a winner–loser crossover, which differs from the winner–winner scheme in InTrance [20]. Exploration is primarily mutation-driven in the present setup.

4.3.3. Crossover

We employ four crossover operators (one-point, uniform, node, and arithmetic) with equal probability (25% each) following Dachwald [95] and Ohndorf [93]. Operator definitions are provided in Appendix B.1.

4.3.4. Mutation

After crossover, each allele $\pi_j \in \pi$ has a predefined probability p_m of being mutated by a factor sampled from a normal distribution $\mathcal{N}(0, \sigma_m)$, where σ_m is the standard deviation of the mutation. Initial conditions are more sensitive to change, thus they are mutated with $\sigma_m/10$.

4.3.5. Staged Optimization and Fixed Launch Parameters

The SOMBRERO runs reported here use two successive optimization stages: (i) exploration with $\sigma_m = 0.1$ and $p_m = 0.1$, and (ii) exploitation initialized from the best exploratory individual with reduced mutation probability $p_m = 0.05$.

For the optimized trajectories from Section 5.2, the optimizer tended toward $\theta_{\text{launch}} \rightarrow 0^\circ$ and $C_3 \rightarrow 0 \text{ km}^2 \text{ s}^{-2}$ across repeated exploratory runs. For computational efficiency, we therefore fix $\theta_{\text{launch}} = 0^\circ$ and $C_3 = 0$ in the reported runs, consistent with the restricted design space stated in Subsection 4.2.

4.3.6. Fitness Functions

The optimization is guided by a staged fitness score $J = \sum_{i=1}^5 j_i$ that enforces the mission sequence before activating the payload objective. The five stages are:

1. **Solar Oberth Maneuver:** Evaluates the spacecraft’s ability to achieve the precise design perihelion ($r_{SOM,design}$) required for the SOM, penalizing deviations.
2. **Approach Jupiter:** Rewards the trajectory for reaching Jupiter’s orbital radius (5.2 AU) post-SOM.

3. **Reaching Solar Escape Velocity:** Ensures the spacecraft possesses sufficient kinetic energy after the Jupiter Gravity Assist (JGA) to achieve solar escape velocity.
4. **Time to 200 AU:** Penalizes solutions that fail to reach the 200 AU target within the 25-year mission constraint.
5. **Maximize Payload Mass:** The final optimization objective, activated only after all preceding constraints are satisfied. This score is directly proportional to the deliverable payload mass (m_{pl}).

This successive evolutionary staging was effective for the present optimization setup. The specific mathematical formulations for each fitness function, along with the criteria for the initial heuristic filter, are detailed in [Appendix B.4](#).

4.4. Simulation Setup

A heliocentric two-body problem low-thrust trajectory simulation environment with dynamic time steps is developed in Python to evaluate trajectories from various steering policies. The initial conditions \mathbf{c}_0 are: launch angle θ_{launch} , hyperbolic excess energy C_3 and combined mass fraction of propellant and payload at launch $\mu_{pp,0}$.

4.4.1. Launch

The spacecraft is launched with an initial mass of m_0 Earth with a launch angle θ_{launch} (counterclockwise positive) with respect to Earth's heliocentric velocity, as shown in Fig. 3.

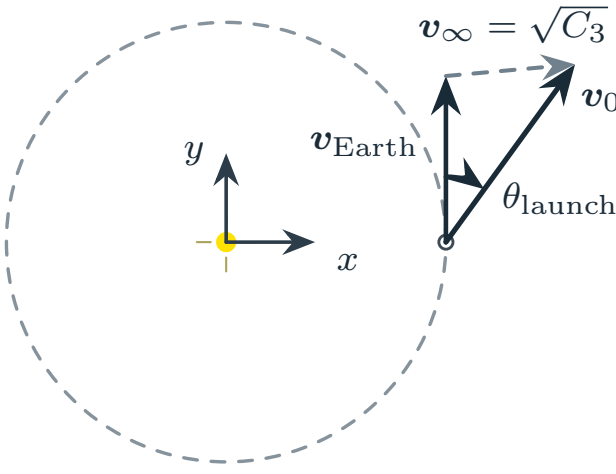


Figure 3: Launch parametrization used in the planar trajectory model. The launch angle θ_{launch} and injected energy C_3 define the initial injection state.

Considering the Earth-relative hyperbolic excess velocity from the launcher $v_{\infty,\text{Earth}} = \sqrt{C_3}$, the initial velocity is given by:

$$\mathbf{v}_0 = \left[-\sin(\theta_{\text{launch}}) v_{\infty,\text{Earth}}, \cos(\theta_{\text{launch}}) v_{\infty,\text{Earth}} + v_{\text{Earth}} \right]^T \quad (3)$$

C_3 determines the initial launch mass [20]:

$$m_0 = m_{0,\text{max}} \exp(-\gamma \cdot C_3) \quad (4)$$

$m_{0,\text{max}} = 15,189$ kg and decay parameter $\gamma = 0.02165 \text{ s}^2 \text{ km}^{-2}$ are derived by fitting conservative performance curves for the fully expendable Falcon Heavy vehicle [100], as shown in [Appendix B.5](#). This model yields slightly lower injected mass estimates than some publicly reported manufacturer performance figures (e.g., > 16.8 t to Mars transfer [101]), thereby introducing an implicit mass margin at the launch interface of around 1.6 t.

4.4.2. Trajectory Propagation

After launch, the spacecraft acceleration $\mathbf{a}_{\text{sc}} = [\ddot{x} \quad \ddot{y}]^T$ is given by the superposition of the sun's gravitational acceleration \mathbf{a}_G and thrust acceleration \mathbf{T}/m_{sc} . Spacecraft steering is achieved through control of the thrust angle θ_T and the power throttling u_P , as shown in Fig. 2.

$$\mathbf{a}_{\text{sc}} = \begin{bmatrix} \ddot{x} \\ \ddot{y} \end{bmatrix} = \mathbf{a}_G + \frac{\mathbf{F}_T}{m_{\text{sc}}} = - \begin{bmatrix} x \\ y \end{bmatrix} \frac{GM_{\odot}}{\sqrt{x^2 + y^2}^3} + \left(\mathbf{n}_T(\theta_T) \frac{2\eta P_{u_P}}{g_0 I_{sp}} \right) / m_{\text{sc}} \quad (5)$$

where x and y are the heliocentric coordinates, GM_{\odot} is the standard gravitational parameter of the Sun, $\mathbf{n}_T(\theta_T)$ is the thrust direction unit vector as a function of the thrust angle θ_T , η is the thrust efficiency, P is the power, u_P is the power throttle, g_0 is the standard gravitational acceleration, and I_{sp} is the specific impulse. The trajectory propagation is carried out using a Runge-Kutta 4 scheme with dynamic timesteps

4.4.3. Jupiter Gravity Assist

When the JGA option is enabled, we apply a planar, instantaneous flyby model in which the post-encounter heliocentric velocity is obtained by rotating the Jupiter-relative velocity vector. Equations and parameter definitions are given in [Appendix B.1.3](#).

5. Results

All results in this section are generated within an idealized planar heliocentric two-body model with no out-of-plane dynamics or ephemeris-based multi-body effects. When included, the JGA follows the analytical in-plane velocity-rotation model of [4.4.3](#). Accordingly, the results should be interpreted as architecture-level performance potential rather than a fully implementable mission design. More exhaustive 3D, ephemeris-based optimization is expected to refine timing and numerical payload values rather than alter the qualitative trade-offs reported here. Model verification and validation are reported in Sections [5.2.3](#) and [5.1](#). The SOMBRERO optimization protocol (including staged exploration/exploitation and fixed launch parameters) is summarized in [4.3.5](#).

5.1. Validation of the SOMBRERO Model

Validation is performed by reproducing the reference SOM+JGA SEP stage from [33, 20] using the same initial conditions (see Appendix B.6.1); the subsequent RTG-powered segment used in [20] to reduce $t_{200\text{AU}}$ is not modeled here. The obtained results are summarized in Table 4.

Table 4: Comparison of InTrance and SOMBRERO for the SOM with Jupiter gravity assist (SOM+JGA) case at $r_{\text{SOM}} = 0.7 \text{ AU}$. Masses refer to the SEP stage. The literature $t_{200\text{AU}}$ includes the additional RTG-powered segment.

Quantity	Literature	This Work	Difference (%)
$v_{\text{post-JGA}} [\text{km s}^{-1}]$	39.3	38.8	-1.3
$\Delta v_{\text{JGA}} [\text{km s}^{-1}]$	12.5	12.3	-1.6
$m_{\text{pl}} [\text{kg}]$	498	464	-6.8
$m_{\text{EPS}} [\text{kg}]$	265	266	0.4
$m_{\text{p}} [\text{kg}]$	440	478	8.6
$m_{\text{s}} [\text{kg}]$	489	491	0.4
$m_0 [\text{kg}]$	1692	1700	0.5
$t_{200\text{AU}} [\text{years}]$	23.8	30.4	27.7

Differences are in general small and can be explained by optimization towards slightly different apohelions. Together with the sub-1 m s^{-1} thrust-integration error reported below, this supports the numerical accuracy of the trajectory propagation (see Appendix B.6.1).

The only notable discrepancy is $t_{200\text{AU}}$, which is not directly comparable here: the reference value includes a subsequent RTG-powered post-SEP stage, whereas the rebuilt case reports the SEP-stage solution and the ensuing ballistic coast. The resulting $\Delta t_{200\text{AU}} \approx 6.6 \text{ yr}$ is therefore expected and consistent with the $\sim 6 \text{ yr}$ reduction attributed to the added RTG stage in [33]. The close agreement in SEP-stage mass and post-JGA velocity in Table 4 supports the accuracy of the core propulsive integration.

5.2. Optimized Trajectories and Mission Profiles

The following subsections detail the trajectory characteristics, steering laws, and mass budgets of the optimized solutions. We first present the mission profile incorporating a Jupiter Gravity Assist (JGA), which yields higher payload but is sensitive to Earth-Jupiter-heliopause phasing and entails additional operational constraints, followed by the direct trajectory scenario, which avoids those constraints at the cost of reduced payload. Based on preliminary exploratory runs, θ_{launch} and C_3 are fixed to 0° and $0 \text{ km}^2 \text{ s}^{-2}$, respectively, as described in Subsection 4.3.5.

5.2.1. Results Incorporating Jupiter Gravity Assist

The optimized SEP-SOM trajectory including JGA delivers 3,083 kg payload to 200 AU in 24.97 years (Fig. 4). Table 5 summarizes the resulting mass and performance breakdown.

The optimized payload mass is nearly two orders of magnitude higher than the 35 kg scientific payload mass found by InTrance for the $r_{\text{SOM}} = 0.7 \text{ AU}$ case. This can be explained by three main factors: i) The reference scenario is launched with

Table 5: Reference-case results summary for the optimized SEP-SOM trajectory including a Jupiter gravity assist.

Quantity	Symbol	Value
Power at 1 AU	P_0	334.2 kW
Perihelion radius	r_{SOM}	0.308 AU
Power at r_{SOM}	P_{\max}	1,954.9 kW
Thrust at r_{SOM}	$F_{T,\max}$	49.8 N
Velocity change	Δv_{EP}	$28,798 \text{ m s}^{-1}$
Jupiter GA velocity change	Δv_{JGA}	$10,627 \text{ m s}^{-1}$
Total launch mass	m_0	15,189 kg
Payload mass	m_{pl}	3,083 kg
Electrical power system mass	m_{EPS}	1,671 kg
Propellant mass	m_{p}	5,878 kg
Structure mass	m_{s}	4,557 kg
Flight time to 200 AU	$t_{200\text{AU}}$	24.97 years
Solar escape velocity	v_{escape}	$9.30 \text{ AU year}^{-1}$

Ariane 5 ($C_3 = 45.1 \text{ km}^2 \text{ s}^{-2}$) and thus offered an m_0 of only 1692 kg, whereas the assumed launch with an expendable Falcon Heavy m_0 is 15,189 kg ($C_3 = 0 \text{ km}^2 \text{ s}^{-2}$). This explains one order of magnitude in difference. The residual order of magnitude is explained by ii) the r_{SOM} at 0.3 AU which is found to offer a significantly stronger solar Oberth effect. This allows for a faster solar escape velocity, which in turn removes the necessity for a REP stage to satisfy the 25 year time limit. Therefore, factor iii) is that the scientific payload is carried directly on the SEP stage in the optimized case presented here, whereas previously the scientific payload had to be carried on board of a further REP stage, such that the payload mass is reduced by the system mass needed for this further stage.

5.2.2. Results for Direct Trajectory

The results of the optimized SOM with no JGA yield a final payload mass of 1,551 kg with 24.34 years of flight time. The trajectory is very similar to the one shown in Fig. 4 and can be found in Appendix B.7.1. The results are summarized in Table 6.

Table 6: Reference-case results summary for the optimized direct SEP-SOM trajectory without a Jupiter gravity assist.

Quantity	Symbol	Value
Power at 1 AU	P_0	424.1 kW
Perihelion radius	r_{SOM}	0.303 AU
Power at r_{SOM}	P_{\max}	2,542.8 kW
Thrust at r_{SOM}	$F_{T,\max}$	64.6 N
Velocity change	Δv_{EP}	$36,191 \text{ m s}^{-1}$
Total launch mass	m_0	15,189 kg
Payload mass	m_{pl}	1,551 kg
Electrical power systems mass	m_{EPS}	2,121 kg
Propellant mass	m_{p}	6,961 kg
Structure mass	m_{s}	4,557 kg
Flight time	$t_{200\text{AU}}$	24.34 years
Solar escape velocity	v_{escape}	$9.03 \text{ AU year}^{-1}$

For context, we compare the SEP-SOM architecture to a

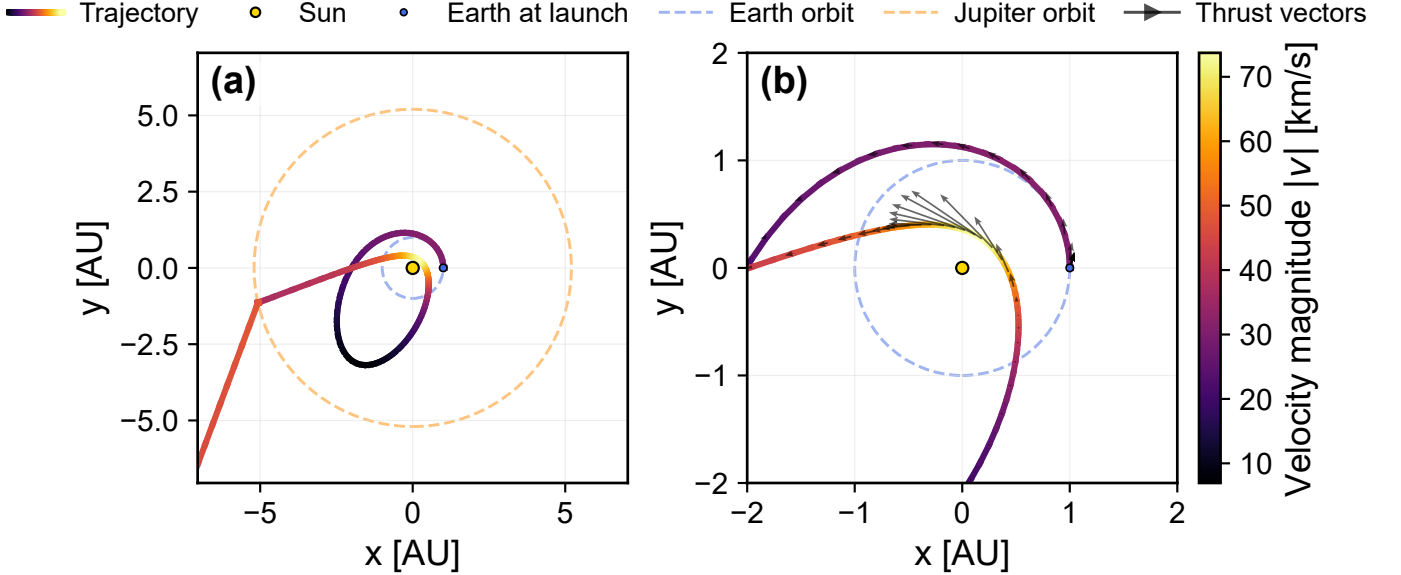


Figure 4: Optimized SEP-SOM trajectory with Jupiter gravity assist. Trajectory in the heliocentric in-plane frame; marker color encodes the heliocentric velocity magnitude $|v|$ (colorbar). Dashed circles indicate the Earth and Jupiter orbits; the blue marker indicates Earth at launch and the yellow disk denotes the Sun. a, Full in-plane trajectory. b, Zoomed view of the near-Sun arc and the Jupiter encounter. SEP, Solar Electric Propulsion; SOM, Solar Oberth Maneuver; JGA, Jupiter gravity assist.

“vanilla” outward electric–propulsion (EP) spiral starting from a circular 1 AU orbit. For the same Δv EP performance, such a reference spiral starting from Earth’s orbit (29.8 km s^{-1}) would yield a heliocentric hyperbolic excess speed of approximately $v_{\infty,\odot} \approx (36.1 - 29.8) \text{ km s}^{-1} \approx 6.3 \text{ km s}^{-1}$, corresponding to 1.33 AU yr^{-1} . The associated increase in specific orbital energy relative to a circular 1 AU orbit is

$$\begin{aligned} \Delta\epsilon_{\text{spiral}} &= \frac{v_{\infty,\odot}^2}{2} + \frac{GM_{\odot}}{2a} \\ &= \frac{(1.33 \times 4,740.47 \text{ m s}^{-1})^2}{2} + \frac{1.3271 \times 10^{20}}{2 \times 1.49598 \times 10^{11}} \text{ m}^2 \text{ s}^{-2} \\ &\approx 4.63 \times 10^8 \text{ m}^2 \text{ s}^{-2}. \end{aligned} \quad (6)$$

For the optimized SEP-SOM trajectory, the corresponding specific orbital energy increment is $\Delta\epsilon_{\text{SEP-SOM}} \approx 1.37 \times 10^9 \text{ m}^2 \text{ s}^{-2}$, i.e. almost a factor of three larger:

$$\frac{\Delta\epsilon_{\text{SEP-SOM}}}{\Delta\epsilon_{\text{spiral}}} \approx 2.95 \approx 3. \quad (7)$$

This illustrates that, for comparable EP capability, the SEP-SOM architecture converts onboard Δv into heliocentric orbital energy significantly more efficiently than a conventional EP spiral.

5.2.3. Verification

The trajectory-propagation and bookkeeping implementation is verified by comparing the Electric Propulsion induced (a) total specific orbital energy change and (b) spacecraft velocity change computed independently via analytical expressions and a discrete numerical approximation for two representative cases (direct and JGA trajectories).

The analytical change in specific orbital energy between the initial circular orbit and solar system escape is given by

$$\Delta\epsilon_{\text{EP,analytic}} = \epsilon_{\text{escape}} - \epsilon_{\text{start}} = \frac{v_{\infty,\odot}^2}{2} - \frac{GM_{\odot}}{2 \cdot 1\text{AU}}, \quad (8)$$

where $v_{\infty,\odot}$ denotes the heliocentric hyperbolic excess speed (distinct from the launcher-provided $v_{\infty,\text{Earth}} = \sqrt{C_3}$).

The specific orbital energy gain from the EP system is evaluated numerically via a discrete approximation

$$\Delta\epsilon_{\text{EP,sim}} = \int_{t_0}^{t_f} \mathbf{a}_{\text{EP}}(t) \cdot \mathbf{v}(t) dt \approx \sum_{i=0}^N \frac{F_{T,i}}{m_{sc,i}} v_i \cos(\theta_{T,i}) \Delta t_i, \quad (9)$$

where $F_{T,i}$ denotes the thrust magnitude at the i -th time step. Similarly, the spacecraft velocity change is determined by two independent methods. First, by numerically integrating the acceleration magnitude, given by

$$\Delta v_{\text{sim}} = \int_{t_0}^{t_f} \frac{F_T(t)}{m_{sc}(t)} dt \approx \sum_{i=0}^N \frac{F_{T,i}}{m_{sc,i}} \Delta t_i. \quad (10)$$

In contrast, the classical Tsiolkovsky equation provides

$$\Delta v_{\text{analytic}} = g_0 I_{sp} \ln \left(\frac{m_{sc,0}}{m_{sc,f}} \right), \quad (11)$$

with $g_0 = 9.81 \text{ m s}^{-2}$ and an effective specific impulse corresponding to 6,000 s.

Furthermore, the specific orbital energy gain due to the JGA maneuver is computed by

$$\Delta\epsilon_{\text{JGA}} = v \Delta v_{\text{JGA}} + \frac{1}{2} \Delta v_{\text{JGA}}^2. \quad (12)$$

Table 7: Analytical versus numerical consistency check for $\Delta\epsilon$ and Δv in the direct and Jupiter-gravity-assist cases.

Quantity	Direct Trajectory	Jupiter Gravity Assist
$\Delta\epsilon_{EP,sim} [\text{J kg}^{-1}]$	1.3653×10^9	9.5907×10^8
$\Delta\epsilon_{JGA,sim} [\text{J kg}^{-1}]$	0	4.5486×10^8
$\Delta\epsilon_{sim} [\text{J kg}^{-1}]$	1.3653×10^9	1.4139×10^9
$\Delta\epsilon_{analytic} [\text{J kg}^{-1}]$	1.3597×10^9	1.4144×10^9
$\Delta\epsilon$ discrepancy [%]	+0.42	-0.03
$\Delta v_{sim} [\text{m s}^{-1}]$	36,190.73	28,798.25
$\Delta v_{analytic} [\text{m s}^{-1}]$	36,086.73	28,770.57
Δv discrepancy [%]	+0.29	+0.10

Table 7 summarizes the results obtained for the two test cases: one without a JGA maneuver (Case 1) and one with an optimized JGA maneuver (Case 2).

The sub-percent agreement between analytical and numerical $\Delta\epsilon$ and Δv estimates supports the numerical consistency of the trajectory propagation and EP/JGA bookkeeping for the considered cases. Residual differences are consistent with finite export resolution and numerical quadrature on rapidly varying high-thrust segments near perihelion, rather than indicating a physical inconsistency.

5.3. Thrust Phasing and Oberth Energy Accumulation

The upper panel of Fig. 5 illustrates how cumulative EP Δv and EP-induced specific orbital energy gain $\Delta\epsilon_{EP}$ accumulate along the optimized SEP–SOM trajectory in the JGA case. The solution applies $\sim 29 \text{ km s}^{-1}$ of EP Δv over the full trajectory, of which $\sim 10 \text{ km s}^{-1}$ are delivered in a short near-perihelion thrust segment. Despite this, the near-perihelion segment produces the dominant increase in EP-induced specific orbital energy gain $\Delta\epsilon_{EP}$, consistent with Eq. (1), which weights the EP energy gain by the instantaneous heliocentric speed.

The lower panel reports the controller outputs, namely thrust angle θ_T and throttle u_P (blue traces in Fig. 5). During the near-perihelion thrust segment, the controller commands near-prograde thrust angles with throttle close to unity, consistent with concentrating propulsion work near perihelion. A repeatable five-phase structure is apparent; the detailed phase breakdown and a qualitative comparison to the no-JGA case are provided in Appendix B.7.2.

5.4. Sensitivity Analysis

The presented results can be generalized beyond the specific mass and power realization by considering conditions under which the same reference trajectory is preserved: (a) identical initial conditions and (b) an identical commanded acceleration vector as a function of time. In the following rescaling map, we vary the system-level α_{EPS} (arrays + PPU, referenced to 1 AU) and μ_s while holding the thruster model parameters ($I_{sp} = 6,000 \text{ s}$, $\eta = 0.75$) fixed; the trajectory and propellant fraction are taken from the optimized reference case and are not re-optimized at each grid point. As shown in Appendix C,

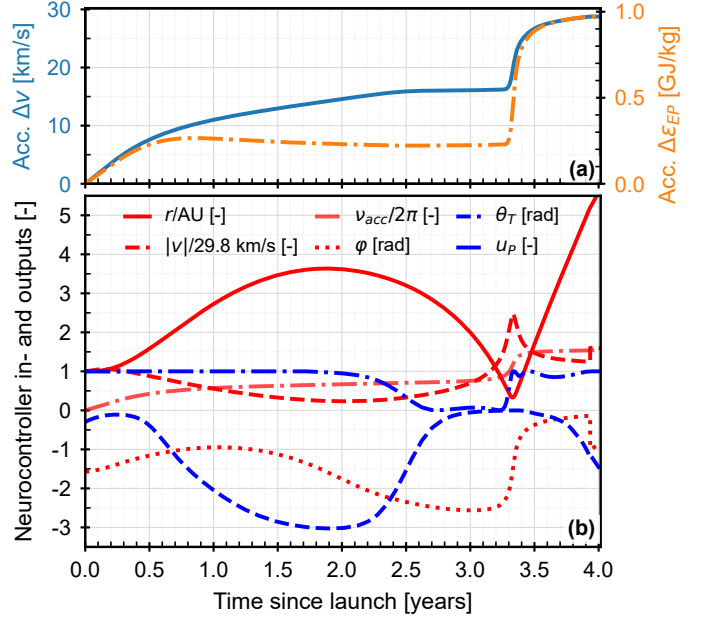


Figure 5: Accumulated electric-propulsion performance and controller signals versus time for the optimized SEP–SOM trajectory in the Jupiter-gravity-assist case. Upper panel: cumulative EP Δv and EP-induced specific orbital energy gain $\Delta\epsilon_{EP}$. Most of $\Delta\epsilon_{EP}$ is accumulated during the short near-perihelion thrust arc, although only part of the total Δv is delivered there. Lower panel: controller inputs (red) and outputs (blue) including thrust angle θ_T and throttle u_P .

this yields a closed-form relation that maps the discrete simulation reference case ($\alpha_{EPS,sim}$, $\mu_{EPS,sim}$, μ_p) to alternative combinations of α_{EPS} and μ_s :

$$m_{pl} = f(m_0, \mu_s, \alpha_{EPS}) \\ = m_0 \left[(1 - \mu_p) - \mu_s - \frac{\alpha_{EPS,sim} \mu_{EPS,sim}}{\alpha_{EPS}} \right] \quad (13)$$

This allows for assessing the payload impact of EPS specific power α_{EPS} and structural mass fraction μ_s under Eq. (13), while keeping the reference propellant fraction μ_p , the thrust history (via the reference trajectory), and the assumed thruster performance fixed. Fig. 6 shows that, at $\mu_s = 0.30$, a 100 kg payload remains feasible for $\alpha_{EPS} \approx 71.80 \text{ W kg}^{-1}$ with a JGA, whereas the direct case requires $\approx 118.78 \text{ W kg}^{-1}$ (a $\sim 1.7\times$ higher specific-power requirement). Relative to the present-day order-of-magnitude EPS-level value $\alpha_{EPS} \approx 78.8 \text{ W kg}^{-1}$ from Section 2.3, these 100 kg thresholds correspond to roughly $0.9\times$ (JGA) and $1.5\times$ (direct), under the additional assumption of 400°C survivability. Ton-class payloads ($\geq 1000 \text{ kg}$) become feasible at $\alpha_{EPS} \approx 89.02 \text{ W kg}^{-1}$ with JGA and $\approx 166.67 \text{ W kg}^{-1}$ without, corresponding to about $1.1\times$ and $2.1\times$, respectively, of that same present-day reference.

6. Discussion

This section discusses the architecture-level implications and main validity bounds of the results.

The SOMBRERO optimization results indicate that, under the baseline assumptions (Section 4.2), a single SEP–SOM at

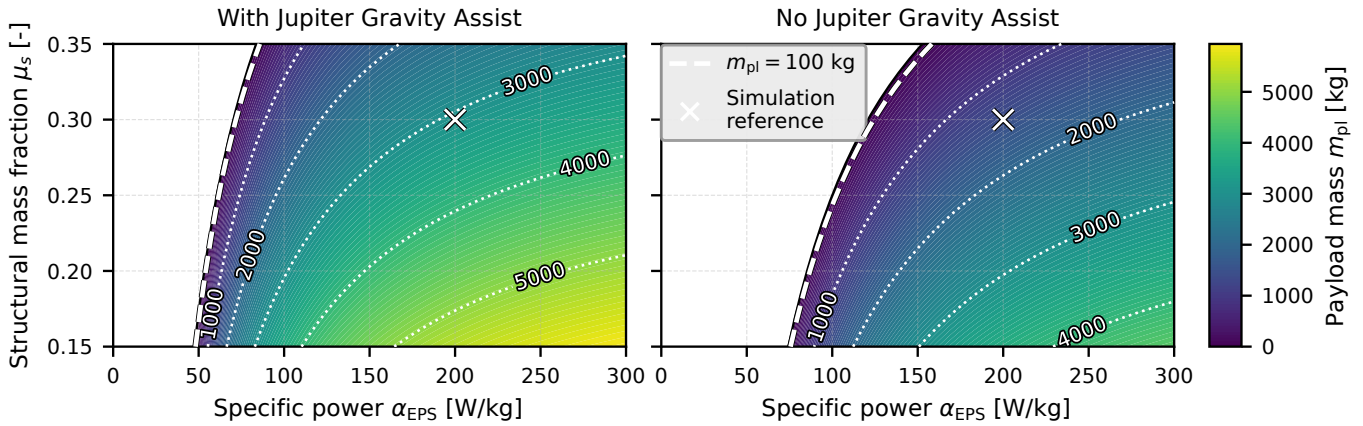


Figure 6: Payload mass sensitivity to EPS specific power α_{EPS} and structural mass fraction μ_s , computed from (13). Left: trajectory including a Jupiter Gravity Assist (JGA). Right: direct trajectory without JGA. Color indicates payload mass m_{pl} in kg. White dotted isolines are spaced by 1,000 kg and labeled. The thin black curve marks the feasibility boundary $m_{\text{pl}} = 0$. The white dashed curve highlights $m_{\text{pl}} = 100$ kg. The white \times denotes the simulation reference at $(\alpha_{\text{EPS}}, \mu_s) = (200 \text{ W kg}^{-1}, 0.30)$. At $\mu_s = 0.30$, the 100 kg isoline intersects $\alpha_{\text{EPS}} \approx 71.80 \text{ W kg}^{-1}$ (with JGA) and $\approx 118.78 \text{ W kg}^{-1}$ (without JGA).

$r_{\text{SOM}} \approx 0.3 \text{ AU}$ launched on an expendable Falcon Heavy can deliver about 3,083 kg of payload to 200 AU in 24.9 yr via a Jupiter Gravity Assist, or 1,551 kg on a direct trajectory in 24.3 yr (Tables 5 and 6). For the same low-thrust Δv , the near-Sun thrust arc yields a heliocentric specific-orbital-energy increase Δe almost three times larger than a 1 AU outward spiral, and Eq. (13) and Fig. 6 further show that payload feasibility spans from near present-day conventional EPS specific-power levels (e.g. $\sim 100 \text{ kg}$ with JGA) to about twice those levels for direct ton-class cases, depending on trajectory class and μ_s .

The subsections below focus on the trade-space shift that occurs when SEP is treated as a short-duration, near-Sun high-power phase, rather than as a continuously power-constrained cruise architecture whose thrust authority rapidly diminishes with heliocentric distance.

6.1. High-Temperature Solar Cells as Interstellar Mission Enablers

High-intensity, high-temperature solar cells have historically been developed for survivability in extreme inner-solar system environments, as reflected in near-Sun mission requirements for high-bandgap devices [49] and modern spacecraft designs (Parker Solar Probe, MESSENGER, Venus probes) [102, 103]. This development focus on thermal survival has resulted in limited assessment of HIHT photovoltaics as propulsion-enabling elements, despite the space-photovoltaics community's emphasis on efficiency, specific power, and radiation hardness [104, 105]. At the same time, trajectory analyses for solar electric Oberth Maneuvers have been limited by the thermal constraints of conventional arrays, restricting prior studies to conservative perihelia of 0.5–0.7 AU [20, 19, 32].

The present study shows that HIHT photovoltaics can shift from a passive role of survival to actively enabling high-power, close-perihelion propulsion architectures for rapid-escape, outer-planet, and interstellar-precursor missions. For example, we describe a 0.3 AU SEP–SOM mission design that has not been explored in detail in the propulsion literature.

6.2. Solar and Nuclear Electric Propulsion: A New Architectural Perspective on Interstellar Precursors

For decades, conceptual studies of fast, interstellar precursor missions have favored Nuclear Electric Propulsion (NEP), widely “advocated as a primary solution” [106] for its distance-independent, high-duty-cycle power [107], while conventional Solar Electric Propulsion (SEP), limited by the inverse-square law, has often been viewed as challenging for outer-solar system missions and considered insufficient for cases like a Pluto orbiter [108]. While this limitation holds for traditional continuous SEP cruise, using SEP as a short-duration, high-power near-Sun phase can reduce its impact. With HIHT photovoltaics, our model of a 0.3 AU EP–SOM provides $\sim 2 \text{ MW}$ near perihelion before coasting, lessening the need for distant solar power. This suggests a possible non-nuclear pathway for high-payload precursor missions when fission-based power is impractical.

Moreover, because the EP–SOM thrust phase spans a significant fraction of the perihelion passage rather than a single impulsive burn, it naturally provides additional freedom to trim injection dispersions and navigation errors as the spacecraft approaches and recedes from perihelion. This mitigates the strong sensitivity to injection errors that characterizes low-perihelion, high-thrust SOM architectures discussed in Section 2.2.

6.3. Implications for Related High-Energy Missions

The high-payload escape capabilities demonstrated in this study (see Tables 5 and 6) also extend to high-energy missions within the solar system. A 0.3 AU SEP–SOM can front-load a large increase in specific orbital energy and may reduce transit times for heavy orbiters toward the ice giants relative to multi-gravity-assist architectures, subject to re-optimization of the outbound leg and arrival conditions.

For outer-planet orbit insertions (e.g. Uranus), a SEP–SOM leg does not inherently impose a large *planetocentric* arrival hyperbolic excess speed $v_{\infty, \text{planet}}$: by re-optimizing the inner-leg

low-thrust steering, one can target a prescribed $v_{\infty, \text{planet}}$, trading longer flight times for higher delivered payload. Because thrusting is confined to the inner solar system, the SEP–SOM sets the outbound heliocentric energy and asymptotic direction, after which the spacecraft coasts ballistically and arrives with a residual velocity mismatch that must be removed during capture. This requires planetocentric Δv not only to eliminate the chosen $v_{\infty, \text{planet}}$ but also to re-orient and reduce the velocity vector to achieve the desired science orbit.

However, the steep decay of solar power with heliocentric distance renders SEP ineffective for short, high- Δv captures at Uranus’ orbit, so a fast SEP–SOM transfer must either constrain v_{∞} to levels manageable by a moderate chemical stage or employ additional technologies such as aerocapture [109]. Alternatively, if nuclear systems are permitted, the same EP thrusters could be powered by a smaller nuclear power source for a prolonged low-thrust spiral capture after the initial SEP–SOM. A full trade of these design options is deferred to future work.

6.4. Validity bounds and limitations

The results are conditional on the simplified feasibility model summarized in Section 4.2 and on the reference technology point used to generate the baseline trajectories. The dominant dependency is the assumed system-level EPS specific power at elevated temperature. The reference case with $\alpha_{\text{EPS}} = 200 \text{ W kg}^{-1}$ is an illustrative anchor rather than a universal feasibility requirement. The sensitivity maps in Section 5.4 quantify how payload degrades with α_{EPS} and μ_s and provide the corresponding threshold interpretation across lower and intermediate specific-power levels. The dynamics and operations are idealized, using planar two-body propagation, an analytical in-plane JGA when applicable, and continuous thrust availability. The high-power EP system is abstracted by constant I_{sp} and η enabled by thruster-string switching over the power envelope. Finally, SOMBRERO is a stochastic optimizer, so the reported steering laws should be interpreted as high-quality near-optimal solutions for the chosen architecture and control parametrization, not strict upper bounds.

7. Conclusions and Future Work

We have presented an architecture-level feasibility study of a high-payload Solar Electric Propulsion Solar Oberth Maneuver (SEP–SOM) for deep-space escape, designed to reduce reliance on nuclear-powered propulsion and to address key limitations of existing deep-space escape concepts such as limited payload capability, complex multi-assist gravity-assist sequences, or the need for costly super-heavy launchers. This design exploits the Oberth effect enabled by emerging high-temperature solar cells, which can power high power Electric Propulsion systems at close solar distances.

Our analysis focuses on a SEP–SOM mission that concentrates low-thrust burns at $\sim 0.3 \text{ AU}$ to maximize payload delivery to 200 AU within 25 yr. Based on laboratory demonstrations of high-temperature solar cells, we adopt a thermal survivability assumption of $\sim 400^\circ\text{C}$ and use a reference EPS

specific power of $\alpha_{\text{EPS}} = 200 \text{ W kg}^{-1}$ at 1 AU as an illustrative high-performance baseline aligned with published development targets for conventional arrays. Spacecraft configuration and steering were optimized using the SOMBRERO evolutionary algorithm under a planar model, and a sensitivity analysis was then used to map payload-feasibility thresholds across lower α_{EPS} values.

Key findings from the baseline analysis are as follows. First, an optimized SEP–SOM (Falcon Heavy launch) can deliver $\approx 3,080 \text{ kg}$ to 200 AU in 24.9 yr (with a Jupiter gravity assist) or $\approx 1,550 \text{ kg}$ in 24.3 yr direct. Second, concentrating thrust near the Sun yields roughly a 3× increase in delivered specific orbital energy versus a 1 AU spiral for the same Δv , providing a primary mechanism behind the SEP–SOM performance gain. Third, the sensitivity maps show that, for the illustrated structural mass fraction case ($\mu_s = 0.30$), payload-feasibility thresholds are near present-day conventional EPS levels for JGA cases and higher than present-day conventional EPS levels for direct cases. Relative to the present-day order-of-magnitude EPS-level value ($\sim 78.8 \text{ W kg}^{-1}$), a 100 kg payload is feasible at roughly $0.9 \times / 1.5 \times$ (JGA/direct), while ton-class payloads ($\geq 1,000 \text{ kg}$) become feasible at roughly $1.1 \times / 2.1 \times$ (JGA/direct). These results define an architecture-level feasibility envelope for non-nuclear high-payload heliopause missions without costly super-heavy launchers (e.g. SLS) under the stated model assumptions.

At the architecture level, these results imply that HIHT solar cells can shift from survival hardware to propulsion-enabling technology for near-Sun Electric Propulsion, providing a novel technology-maturation rationale. Using SEP only as a short, high-power phase (front-loading Δv) offers a potential non-nuclear (electric) propulsion approach for interstellar precursors. This near-Sun energy front-loading concept may also apply to fast outer-planet or high- Δv missions. Under the reference-case assumptions, a single near-Sun SEP–SOM could thus provide a high-payload precursor trajectory to the heliopause with one Falcon Heavy.

Future work should focus on three extensions. First, translate EPS assumptions from cell-level HIHT demonstrations to panel- and system-level designs, including temperature-dependent degradation, integration penalties, and explicit margins. Second, extend the optimization to multi-architecture trades across payload, transfer time, perihelion distance, launch energy, and alternative high-power EP options to identify regimes where SEP–SOM is competitive compared with multi-assist or nuclear electric solutions. Third, move from planar two-body dynamics to 3D, ephemeris-based optimization with operational and navigation constraints to quantify robustness to dispersions and feasibility under guidance, thermal, and pointing limits.

Taken together, these steps would help translate the trajectory-level performance trends established here into more detailed mission designs. If the assumed HIHT array performance can be realized at panel level with credible margins, we suggest that low-perihelion SEP–SOM be considered among candidate architectures for interstellar precursor and other high-energy deep-space missions.

Abbreviations

AF-	Applied-Field	Magnetoplasmadynamic
MPD	Thruster	
ANN	Artificial Neural Network	
COTS	Commercial Off-The-Shelf	
EGA	Earth Gravity Assist	
ENC	Evolutionary Neuro-Control	
EP	Electric Propulsion	
EPS	Electrical Power System	
GIT	Gridded Ion Thrusters	
HIHT	High-Intensity High-Temperature	
JGA	Jupiter Gravity Assist	
LEO	Low Earth Orbit	
NTP	Nuclear Thermal Propulsion	
NTR	Nuclear Thermal Rocket	
PPU	Power Processing Unit	
REP	Radioisotope Electric Propulsion	
RTG	Radioisotope Thermal Generator	
SEP	Solar Electric Propulsion	
SOM	Solar Oberth Maneuver	
SLS	Space Launch System	
STP	Solar Thermal Propulsion	
TRL	Technology Readiness Level	
VGA	Venus Gravity Assist	

Symbols

Sym.	Definition	Unit
a	semi-major axis	[AU]
c_0	initial conditions	N/A
C_3	characteristic energy	[km ² s ⁻²]
F_T	thrust magnitude	[N]
GM	gravitational parameter	[m ³ s ⁻²]
I_0	solar irradiance at 1 AU	[W m ⁻²]
I_{sp}	specific impulse	[s]
J	fitness score	[–]
j_i	sub-fitness scores	[–]
m_0	launch mass	[kg]
m_{dry}	delivered dry spacecraft mass	[kg]
m_{EPS}	mass of EPS	[kg]
m_p	propellant mass	[kg]
m_{pl}	allocatable mission payload mass	[kg]
m_s	structure mass	[kg]
m_{sc}	instantaneous spacecraft mass	[kg]
P	power	[W]
$P(\chi)$	steering policy	[–]
p_m	mutation probability	[–]
R_\odot	solar radius	[km]
r_{JGA}	periapsis distance for JGA	[km]
r_{SOM}	distance at SOM perihelion	[AU]
T	temperature	[K]
t_{200AU}	flight time to 200 AU	[years]
\mathbf{u}	steering control commands	[–]
u_P	throttle command	[–]

Sym.	Definition	Unit
v	orbital velocity	[km s ⁻¹]
v_{escape}	solar system escape velocity	[AU s ⁻¹]
v_∞	hyperbolic excess velocity	[AU s ⁻¹]
α	specific power	[W kg ⁻¹]
γ	decay parameter	[s ² km ⁻²]
Δv	orbital velocity increment	[km s ⁻¹]
δ	turn angle for gravity assist	[rad]
ϵ	emissivity	[–]
ε	specific orbital energy	[MJ kg ⁻¹]
η	efficiency	[–]
θ_T	thrust angle	[rad]
κ	scaling component for EPS power	[–]
μ	mass fraction	[–]
ν	true anomaly	[rad]
ξ	ANN genetic material parameter	[–]
π	ANN genetic chromosome	[–]
σ	gaussian-type activation functions	[–]
φ	flight path angle	[rad]
χ	spacecraft state	[–]

CRediT Authorship Contribution Statement

- **N. Maraqtan:** Conceptualization; Project Administration; Methodology; Software; Formal analysis; Investigation; Data curation; Visualization; Writing – original draft; Writing – review & editing.
- **W. van Lynden:** Investigation (literature review on high-temperature solar arrays and electric propulsion technologies); Writing – original draft (background subsections, discussion subsections); Writing – review & editing.
- **C. Gómez de Olea Ballester:** Investigation (literature review on Solar Oberth maneuvers and high-temperature solar cells); Visualization; Writing – original draft (background subsections, discussion subsections); Writing – review & editing.
- **A. Hein:** Supervision; Writing – review & editing.

Data Availability

The curated supporting artifacts (Excel trajectory time-series and scalar summaries for the JGA, no-JGA, and InTrance verification cases) are available in the public SOMBRERO repository at [\[GITHUB_URL\]](#) under `data/paper_artifacts/`. These are cross-check artifacts; primary reproduction of the reported reference trajectories is via the configuration files and optimized chromosomes provided under `configs/`, using the `simulate` command documented in the repository README.

Code Availability

The SOMBRERO trajectory optimization and simulation code used in this study is publicly available under the MIT License at [\[GITHUB_URL\]](#). The repository includes configuration

files, optimized neural-network chromosomes, and installation instructions for hot-start reconstruction of the two paper reference trajectories (Tables 5 and 6). Reproducibility scope and platform-dependence notes are provided in the repository documentation.

Declaration of Generative AI and AI-assisted technologies in the writing process

During the preparation of this work the authors used Gemini 3 and GPT 5.2 in order to improve language and readability. After using these tools/services, the authors reviewed and edited the content as needed and take full responsibility for the content of the publication.

Declaration of Competing Interest

The authors declare that they have no known competing financial interests or personal relationships that could have appeared to influence the work reported in this paper.

Funding

This research did not receive any specific grant from funding agencies in the public, commercial, or not-for-profit sectors.

Appendix A. Supplementary literature review: non-electric SOM propulsion

This appendix provides additional discussion of non-electric SOM implementations (chemical, solar sail, solar thermal, and nuclear thermal), complementing Table 1. The main text focuses on electric-propulsion SOM architectures.

Appendix A.1. Chemical Propulsion SOM

Chemical Solar Oberth Maneuvers have been studied for high-energy, long-range missions (see Table 1), with targets ranging from the heliopause (~ 100 AU) [7] to encounters with the hypothetical Planet 9 (~ 400 AU) [29] or interstellar objects such as 3I/Atlas [34]. Across these scenarios, mass constraints remain the principal limitation. Reported delivered payloads vary from ~ 100 kg [29] to ~ 500 kg [34], though in reality these numbers would be reduced by the parasitic heat shield mass, which is expected to consume a significant fraction of the payload due to the extremely low perihelion conditions. For instance, in Hopkins et al.'s concept [7], the reported delivered dry spacecraft mass is ~ 380 kg, while the low perihelion (11 solar radii) thermal environment for the SOM requires a ~ 300 kg heat shield. In comparison, perihelion conditions in the scenarios reported by Hibberd et al. [29] and Hibberd & Eubanks [34] are even more extreme, implying an even larger fraction of the payload could be consumed by thermal protection.

Appendix A.2. Solar Sail Propulsion SOM

Highly reflective solar sails can harness radiation pressure to accelerate spacecraft, with closer perihelia providing higher Δv through a Solar Oberth Maneuver [30]. Lightweight sails with large area-to-mass ratios could enable velocities exceeding 20 AU year^{-1} (more than 5 times that of Voyager I) for perihelia as low as 0.05 AU. Mass remains a key constraint, often requiring sail areas $> 10,000 \text{ m}^2$ even for delivered dry spacecraft masses of 10–50 kg [15, 30]. Concepts such as a ~ 400 m sail carrying a 25 kg *science payload* illustrate the scale of the required deployable structures (see Table 1).

Solar sailing has progressed from concept to demonstration, including IKAROS (16 kg, 200 m^2), NanoSail-D, LightSail 1/2, and the upcoming NASA Solar Cruiser (~ 100 kg, $1,700 \text{ m}^2$) [30, 110]. Future proposals suggest extreme solar flybys ($< 5 R_\odot$) could accelerate 10–20 kg spacecraft to $\sim 60 \text{ AU year}^{-1}$ ($\approx 0.001c$), reaching Neptune in 10 months or 1,000 AU in 17 years, with swarm formation enabling larger effective payloads [31].

Laser-driven sails offer an alternative, using Earth-based high-power lasers for acceleration. Hibberd et al. [36] studied gram-to-kilogram-class spacecraft to intercept 1I/'Oumuamua at $0.001c$, reaching ~ 82 AU in 444 days after a SOM at 3 solar radii. Payload and infrastructure remain limiting factors.

Appendix A.3. Solar Thermal Propulsion (STP)

Solar Thermal Propulsion (STP) converts radiant solar energy into thermal energy, which is then transformed into kinetic energy to provide thrust, offering at least double the specific impulse of chemical propulsion under conservative assumptions [111] and enabling high-energy Solar Oberth Maneuvers at low perihelia [26, 37] (see Table 1).

Early conceptual studies demonstrated velocities above 11 AU year^{-1} for perihelia ~ 0.02 AU [37], while later designs, such as a 50 kg probe performing a Jupiter flyby and perihelion burn at $3\text{--}4 R_\odot$, could reach 20 AU year^{-1} [26]. Sauder et al. [27] showed that a 478 kg probe could achieve $8 - 10 \text{ AU year}^{-1}$ with a 36 kg *science payload*, and hybrid architectures combining STP with nuclear-electric or advanced ion propulsion could push velocities to $19.5 - 21 \text{ AU year}^{-1}$. Benkoski et al. [14] experimentally demonstrated hardware capable of 15 AU year^{-1} for $2.5 R_\odot$ perihelia, though payload remains heavily constrained by thermal protection and cooling requirements.

Appendix A.4. Nuclear Thermal Propulsion SOM

Nuclear Thermal Propulsion (NTP) has been studied for fast interstellar precursor missions, combining SLS launches with perihelion Solar Oberth Maneuvers (see Table 1). Hibberd & Hein [28] analyse fast intercept missions to interstellar object 1I/'Oumuamua, with a potential LEO \rightarrow SOM \rightarrow 1I trajectory achieving 1.3 t (no JGA) to 7.8 t (with JGA) spacecraft masses over 21 to 32 years, though residual mass available for payload is very limited. Irvine et al. [38] evaluate NTR missions to the heliopause and beyond, showing that an SLS Block 1 plus a $10 R_\odot$ perihelion burn can reach $43 - 59.8 \text{ km s}^{-1}$ exit velocities, enabling 500 AU in 32 years, again with limited payloads.

Appendix B. Supplementary material: SOMBRERO implementation and supporting models

This appendix collects implementation-level details needed to reproduce the SOMBRERO results. Neurocontrol and fitness definitions are given in [Appendix B.1](#) and [Appendix B.4](#). Supporting models and fits are documented in [Appendix B.5](#), [Appendix B.2](#), [Appendix B.3](#), and [Appendix B.1.3](#). Verification, validation, and the no-JGA ablation case are reported in [Appendix B.6](#), [Appendix B.7.1](#), and [Appendix B.7.2](#).

Appendix B.1. Evolutionary neurocontrol method definitions

Appendix B.1.1. Activation functions

The Gaussian-type activation functions

$$\sigma_{\theta_T}(x) = -\exp(-x^2), \quad \sigma_{u_P}(x) = 1 - \exp(-5x^2) \quad (\text{B.1})$$

in the output layer, along with the $\sigma_h(x) = \tanh(x)$ functions in the hidden layer, facilitated the learning process. σ_{θ_T} and σ_{u_P} are designed to match the expected behavior of $u_P \rightarrow 100\%$ and $\theta_T \rightarrow 0$ in the most critical point of the trajectory, the SOM perihelion, when receiving similar input states. This simplifies learning by limiting the solution space to negative θ_T .

Appendix B.1.2. Crossover

Crossover is a genetic operator used to combine the genetic information of two parents to produce offspring. In the SEP-SOM context, crossover was conducted with a probability of 25% [95]:

- **One Point Crossover:** A single crossover point on each chromosome is chosen. The data beyond that point in either chromosome is swapped between the two parent chromosomes.
- **Uniform Crossover:** Each gene in the offspring is randomly chosen from the corresponding genes of the parents, with equal probability.
- **Node Crossover:** Nodes from both parents are randomly selected and swapped, helping the offspring inherit structural properties from both parents.
- **Arithmetic Crossover** Offspring are created by performing a weighted average of the parent chromosomes. The weight is randomly selected.

The best practice recommendations of keeping information of the winner are kept. Therefore only nodes and node information (weights, bias) are considered [93].

Appendix B.1.3. Jupiter Gravity Assist Model

A Jupiter Gravity Assist (JGA) maneuver is implemented as described by [112]. The process is summarized below:

In this planar analysis, the JGA is modeled as an instantaneous change in the spacecraft's heliocentric velocity at Jupiter's orbital radius. This simplification neglects three-dimensional effects and finite-duration flyby arcs but captures the principal energy gain mechanism. The periapsis distance

of the JGA is fixed, and the spacecraft's approach is assumed to occur at Jupiter's orbital radius. Though a fixed periapsis assumption may not be optimal, the resulting energy gain established here remains valid for the optimal-phasing case.

The spacecraft's position and velocity are represented by (x, y) and (\dot{x}, \dot{y}) , respectively, in a heliocentric inertial frame. The relative velocity of the spacecraft with respect to Jupiter is computed as:

$$\mathbf{v}_{\text{relative}} = \mathbf{v}_{\text{sc}} - \mathbf{v}_{\text{Jupiter}} \quad (\text{B.2})$$

where \mathbf{v}_{sc} is the spacecraft's heliocentric velocity and $\mathbf{v}_{\text{Jupiter}}$ is Jupiter's heliocentric velocity vector. The turn angle δ for the gravity assist is determined by:

$$\delta = 2 \arcsin \left(\frac{1}{1 + \frac{r_{\text{JGA}} \cdot \|\mathbf{v}_{\text{relative}}\|^2}{GM_{\text{Jupiter}}}} \right) \quad (\text{B.3})$$

where r_{JGA} is the periapsis distance of the JGA, $\mathbf{v}_{\text{relative}}$ is the magnitude of the spacecraft's velocity relative to Jupiter, and GM_{Jupiter} is the gravitational parameter of Jupiter.

A rotation matrix is applied to the relative velocity vector to compute the final velocity after the JGA:

$$\mathbf{R}_\delta = \begin{bmatrix} \cos(\delta) & -\sin(\delta) \\ \sin(\delta) & \cos(\delta) \end{bmatrix} \quad (\text{B.4})$$

$$\mathbf{v}_{\text{final}} = \mathbf{R}_\delta \cdot \mathbf{v}_{\text{relative}} + \mathbf{v}_{\text{Jupiter}} \quad (\text{B.5})$$

where $\mathbf{v}_{\text{final}}$ is the final velocity of the spacecraft after the gravity assist, and $\mathbf{v}_{\text{Jupiter}}$ is Jupiter's heliocentric velocity vector. The periapsis distance r_{JGA} is assumed to be 1.34 Jupiter radii [93].

Appendix B.2. MESSENGER spacecraft structural mass fraction estimate

SMAD Table A-10 reports for MESSENGER $m_0 = 1102$ kg, $m_{\text{dry}} = 508$ kg, $m_{\text{pl}} = 47$ kg, and an electric power system mass share of $\tilde{\mu}_{\text{EPS}} = 0.24$ given as a fraction of dry mass [98]. Using the paper bookkeeping $m_{\text{dry}} = m_{\text{pl}} + m_{\text{EPS}} + m_s$, we set $m_{\text{EPS}} = \tilde{\mu}_{\text{EPS}} m_{\text{dry}}$ and obtain the launch-mass structural fraction

$$\begin{aligned} \mu_{s,0} &\equiv \frac{m_s}{m_0} = \frac{m_{\text{dry}} - m_{\text{pl}} - \tilde{\mu}_{\text{EPS}} m_{\text{dry}}}{m_0} \\ &= \frac{508 - 47 - 0.24 \cdot 508}{1102} = 0.30770. \end{aligned} \quad (\text{B.6})$$

Appendix B.3. Temperature-limited perihelion scaling

This appendix summarizes the radiative-equilibrium argument used to relate a temperature limit of the photovoltaic system to a minimum feasible SEP-SOM perihelion distance.

We model the incident solar irradiance as $I(r) = I_0/r^2$, with r in astronomical units and I_0 the solar constant at 1 AU. For a panel with net absorbed heat flux $\alpha_{\text{net}}I(r)$, radiative equilibrium with emission from the front and rear sides gives [96, 17]

$$\alpha_{\text{net}} \frac{I_0}{r^2} = (\epsilon_f + \epsilon_r) \sigma T^4, \quad (\text{B.7})$$

where ϵ_f and ϵ_r are the front- and rear-side hemispherical emissivities, $\sigma = 5.670374419 \times 10^{-8} \text{ W m}^{-2} \text{ K}^{-4}$ is the Stefan-Boltzmann constant, T is the panel operating temperature (in K), and α_{net} denotes the net fraction of incident irradiance converted to heat (absorptance minus electrical conversion efficiency). Rearranging yields the scaling

$$r_{\text{SOM}} = \sqrt{\frac{\alpha_{\text{net}}}{\epsilon_f + \epsilon_r}} \frac{I_0}{\sigma} \frac{1}{T^2}, \quad (\text{B.8})$$

i.e. $r_{\text{SOM}} \propto T^{-2}$ for fixed optical properties.

A commonly used simplifying case is $\alpha_{\text{net}} = \epsilon_f = \epsilon_r$, corresponding to symmetric emission from both sides. In contrast, if only one side effectively emits, the denominator reduces from $(\epsilon_f + \epsilon_r)$ to a single emissivity, which increases the implied perihelion distance by a factor $\sqrt{2}$ for the same T and α_{net} . In the main text, this range is used only to motivate the representative baseline choice $r_{\text{SOM}} = 0.3 \text{ AU}$ for $T \approx 400^\circ\text{C}$.

Appendix B.4. Fitness function formulations and heuristics

This appendix provides the detailed mathematical definitions and heuristic filters used within the evolutionary neurocontrol framework, as introduced in Section 4.3.

Appendix B.4.1. Heuristic Filter for SOM Candidates

To accelerate convergence and prune the search space of unfit individuals, a heuristic filter is applied after the first generation. Only individuals exhibiting viable SOM characteristics (termed “SOM candidates”) are allowed to “survive” and be passed to the next generation. Individuals that fail to meet these criteria are re-initialized. This pre-selection process, based on characteristics expected from a successful SOM trajectory, significantly decreases dependence on the randomly initialized first generation.

The criteria for this filter are:

- (a) Average heliocentric distance $r_{\text{avg}} > 1.2 \text{ AU}$.
- (b) The trajectory must contain only one local maximum in r .
- (c) The local maximum in r must be greater than 2 AU.
- (d) The final radial distance $r_{\text{final}} > 1 \text{ AU}$ after 4.5 years of simulation.

Appendix B.4.2. Staged Fitness Function Definitions

SOM candidates enter the main evolutionary loop, where their performance is evaluated based on the five successive stages described in the main text. The mathematical formulation for each sub-fitness score j_i is as follows:

- Solar Oberth Maneuver:** This phase evaluates the spacecraft’s ability to achieve a minimal distance r_{min} that matches the design perihelion $r_{\text{SOM,design}}$, with penalties for deviations. This evolutionary stage is considered passed if $0.2 \text{ AU} < r_{\text{min}} < 0.6 \text{ AU}$.

$$j_1(r_{\text{min}}) = \begin{cases} \exp(-1000(r_{\text{min}} - r_{\text{SOM,design}})) & \text{if } r_{\text{min}} < r_{\text{SOM,design}} \\ \exp(-(r_{\text{min}} - r_{\text{SOM,design}})^2) & \text{if } r_{\text{min}} \geq r_{\text{SOM,design}} \end{cases} \quad (\text{B.9})$$

- Approach Jupiter:** After the SOM, the j_2 score rewards reaching a maximal radial distance r_{max} near Jupiter’s orbit (5.2 AU).

$$j_2(r_{\text{max}}) = \begin{cases} \frac{r_{\text{max}}}{5.2} & \text{if } r_{\text{max}} < 5.2 \text{ AU} \\ 1 & \text{if } r_{\text{max}} \geq 5.2 \text{ AU} \end{cases} \quad (\text{B.10})$$

- Reaching Solar Escape Velocity:** After the JGA, the spacecraft velocity v must be at or above the escape velocity from Jupiter’s orbit (5.2 AU) $v_{\text{escape,J}} = 18471 \text{ m s}^{-1}$. The j_3 score rewards kinetic energies approaching this threshold.

$$j_3(v) = \begin{cases} \frac{v^2}{v_{\text{escape,J}}^2} & \text{if } v < 18471 \text{ m s}^{-1} \\ 1 & \text{if } v \geq 18471 \text{ m s}^{-1} \end{cases} \quad (\text{B.11})$$

- Time to 200 AU:** The spacecraft must reach 200 AU within 25 years. The j_4 score rewards smaller t_{200AU} . This stage is considered passed when the target time is reached.

$$j_4(t_{200AU}) = \begin{cases} -\tanh(0.5(\frac{t_{200AU}}{25 \text{ years}} - 1)) + 1 & \text{if } t_{200AU} > 25 \text{ years} \\ 1 & \text{if } t_{200AU} \leq 25 \text{ years} \end{cases} \quad (\text{B.12})$$

- Maximize Payload Mass:** This final phase, activated when $J \geq 4$, focuses on maximizing the payload mass m_{pl} . The score j_5 is equivalent to m_{pl} in units of 1000 kg.

$$j_5(m_{pl}) = m_{pl}/1000 \text{ kg} \quad (\text{B.13})$$

Appendix B.5. Launch

Using Falcon Heavy (expendable) data from [100] a fit of

$$m_0 = m_{0,\text{max}} \exp(-\gamma \cdot C_3) \quad (\text{B.14})$$

yields $m_{0,\text{max}} = 15,189 \text{ kg}$ and $\gamma = 0.02165 \text{ s}^2 \text{ km}^{-2}$, as shown in Fig. B.7.

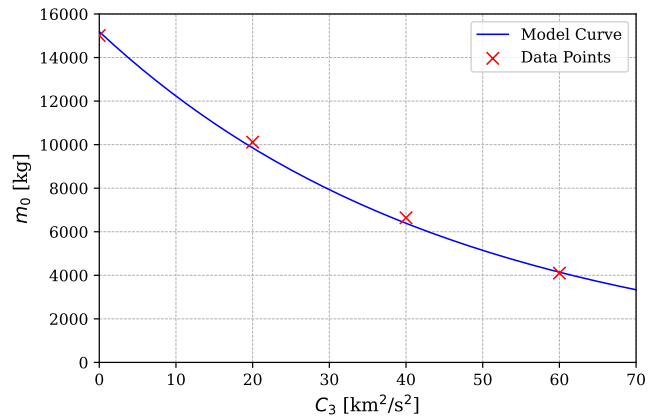


Figure B.7: Injected mass model for an expendable Falcon Heavy as a function of launch energy C_3 , used in this study.

Table B.8: Initial and boundary conditions for the literature reference SOM case with $r_{\text{SOM}} = 0.7 \text{ AU}$ used in the validation study.

Parameter	Value	Parameter	Value
I_{sp}	7,377 s	Launcher	Ariane 5
η	71.6%	C_3	$45.1 \text{ km}^2 \text{ s}^{-2}$
P_0 (1 AU)	53 kW	μ_{EPS}	0.157
α	200 W kg^{-1}	μ_s	0.289

Appendix B.6. Validation

Appendix B.6.1. Rebuilding Literature Results

Initial conditions from [20, 33] are shown in Table B.8.

The subsystem mass fraction, μ_s , stems from the assumed fixed-thrust units (6 RIT-22 + power units), the Xenon tank, and the supporting structure, which together amount to

$$m_s = 224 \text{ kg} + 26 \text{ kg} + 239 \text{ kg} = 489 \text{ kg} \quad (\text{B.15})$$

leading to $\mu_s = 0.289$ (489 kg out of 1,692 kg) [33]. Note that Loeb et al. do not assume an initially combined propellant mass fraction,

$$\mu_{pp} = 1 - \mu_s - \mu_{EPS} \quad (\text{B.16})$$

as part of the optimized initial conditions \mathbf{c}_0 . Instead, they assume a characteristic power fraction of

$$P_c = 65\%, \quad (\text{B.17})$$

which is defined as the percentage of power at 1 AU relative to the maximum power available at perihelion, in the case of the six RIT22 thrusters: $P_m = 6 \cdot 13.59 \text{ kW}$. This assumption determines the electrical power system (EPS) mass fraction as

$$\mu_{EPS} = \frac{P_{\max} P_c}{\alpha m_0} = \frac{81.54 \text{ kW} \cdot 0.65}{200 \text{ W kg}^{-1} \cdot 1,692 \text{ kg}} \approx 0.157. \quad (\text{B.18})$$

Trajectory from [20], overlaid with the trajectory from the SOMBREERO tool, is shown in Fig. B.8. The optimized trajectory (dashed line) here is close to the one reported by Ohndorf et al. (solid line). Small deviations in the apohelion result in differences in the final payload and propellant masses (see Tab. 4). These deviations can be attributed to differences in the optimization approaches: InTrance uses a high-fidelity model that explicitly simulates Earth and Jupiter as moving bodies, requiring the trajectory to optimize an active "catch" of Jupiter for a gravity assist. In contrast, SOMBREERO simplifies the problem by considering only the orbital radii and automatically applying an analytical gravity assist once the 5.2 AU threshold of Jupiter's orbit is reached. This reduced complexity in the optimization case, by eliminating the need to precisely target Jupiter, may lead to the observed differences.

Appendix B.6.2. Thrust Acceleration Error Assessment

A further confirmation of the simulation accuracy is provided by a detailed thrust acceleration error assessment. The analytical velocity increment is computed using Tsiolkovsky's rocket

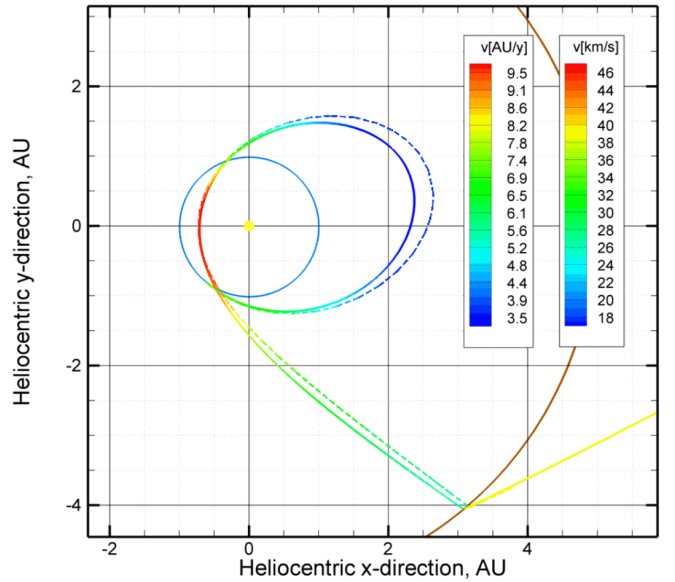


Figure B.8: Overlay of heliocentric in-plane trajectories for the reference SOM case. Solid line: InTrance result from Ohndorf et al. [20]. Dashed line: SOMBREERO reproduction under the same initial conditions. The close agreement supports the reconstructed baseline trajectory.

equation [113]:

$$\begin{aligned} \Delta v_{\text{analytical}} &= g I_{sp} \ln\left(\frac{m_0}{m_0 - m_p}\right) \\ &= 9.81 \text{ m s}^{-2} \cdot 7,377 \text{ s} \cdot \ln\left(\frac{1,700.430 \text{ kg}}{1,700.430 \text{ kg} - 478.245 \text{ kg}}\right) \\ &\approx 23,899 \text{ m s}^{-1}. \end{aligned}$$

This result is compared with the simulation output, where the velocity increment is obtained by numerically integrating the thrust acceleration:

$$\Delta v_{\text{sim}} = \int_0^{t_{\text{final}}} \frac{|F_T(t)|}{m_{sc}(t)} dt \approx \sum_{i=0}^n \frac{|F_T(t_i)|}{m_{sc}(t_i)} \Delta t_i \approx 23,899 \text{ m s}^{-1}.$$

Thus, the absolute error is given by

$$|\Delta v_{\text{analytical}} - \Delta v_{\text{sim}}| < 1 \text{ m s}^{-1},$$

confirming that the thrust acceleration is accurately simulated.

Appendix B.7. Optimization Reference Case Without Jupiter Gravity Assist

Appendix B.7.1. Trajectory

Figs. B.9 shows the trajectory without JGA.

Appendix B.7.2. Learned Strategy

Figure B.10 shows the learned steering policy for the SEP-SOM trajectory without a Jupiter gravity assist. The neurocontroller maps the state to controls according to the policy encoded by its neural network genome ξ , yielding thrust angle θ_T and throttle u_P over mission time t . The upper panel tracks the

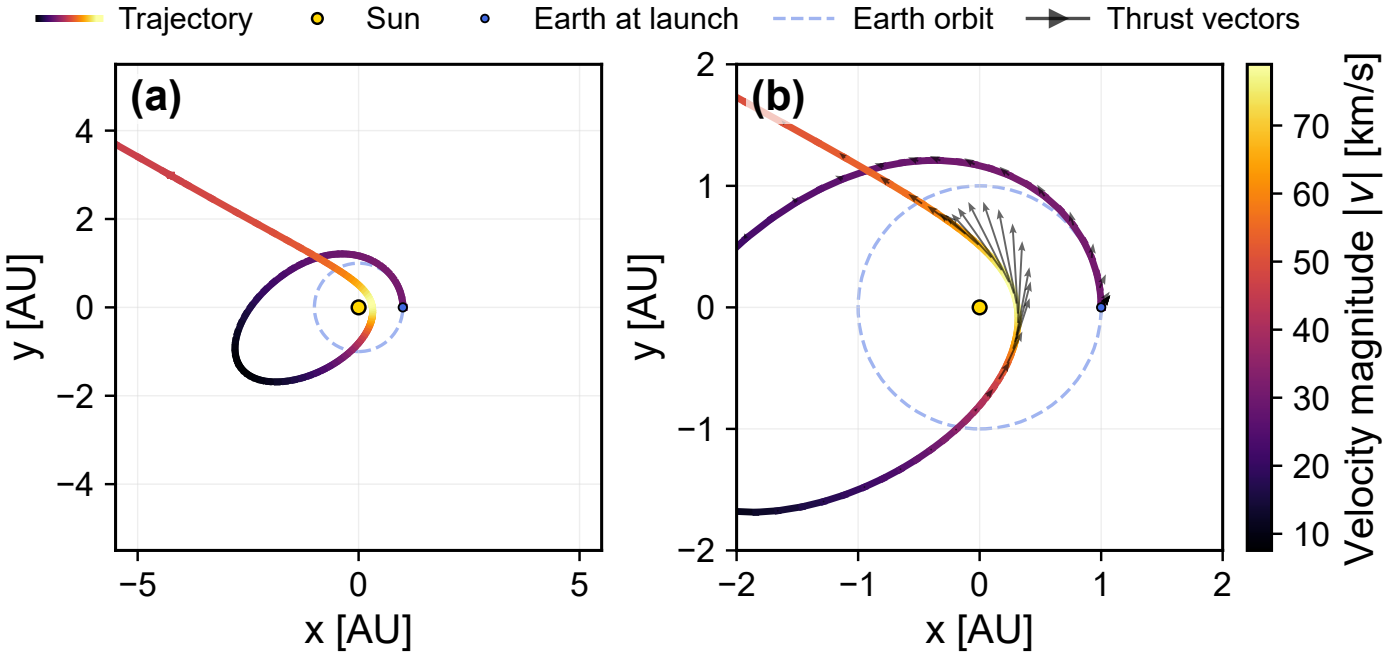


Figure B.9: Optimized SEP–SOM trajectory without Jupiter gravity assist. Trajectory in the heliocentric in-plane frame; marker color encodes the heliocentric velocity magnitude $|v|$ (colorbar). The dashed circle indicates the Earth orbit; the blue marker indicates Earth at launch and the yellow disk denotes the Sun. a, Full in-plane trajectory. b, Zoomed view of the near-Sun arc. SEP, solar electric propulsion; SOM, solar Oberth maneuver.

cumulative electric-propulsion Δv and the corresponding EP-induced specific orbital energy gain $\Delta \varepsilon_{EP}$. The lower panel shows selected controller inputs (red) as well as outputs (blue), namely θ_T and u_P .

The controller maintains a power throttle $u_P = 1$ and a thrust angle of 0° during the solar Oberth maneuver. The policy thus concentrates electric-propulsion work in the high-velocity arc around perihelion, consistent with the continuous Oberth effect relation in Eq. (1).

By inspecting thrust direction and throttle level in Fig. B.10, the qualitative phase structure remains similar to the JGA case. Five phases can be identified:

1. **Apohelion raise (0.0–0.6 yr).** Full throttle, prograde pointing to raise apohelion.
2. **Perihelion decrease (0.6–1.8 yr).** Near-full throttle, retrograde pointing to drive perihelion to the design value.
3. **Coast (1.8–2.3 yr).** Throttle near zero to set up the solar passage.
4. **Solar Oberth (2.3–2.55 yr).** Full-power, prograde thrust through perihelion, consistent with the continuous Oberth energy accumulation in Eq. (1).
5. **Post-SOM outbound arc (2.55–3.0 yr).** A follow-on thrust segment. In the no-JGA case, the controller maintains $u_P \approx 1$ directly after perihelion, thereby extending high-power thrusting into the post-perihelion arc.

A qualitative comparison to the JGA case in Fig. 5 indicates that the main difference lies in the post-perihelion throttle be-

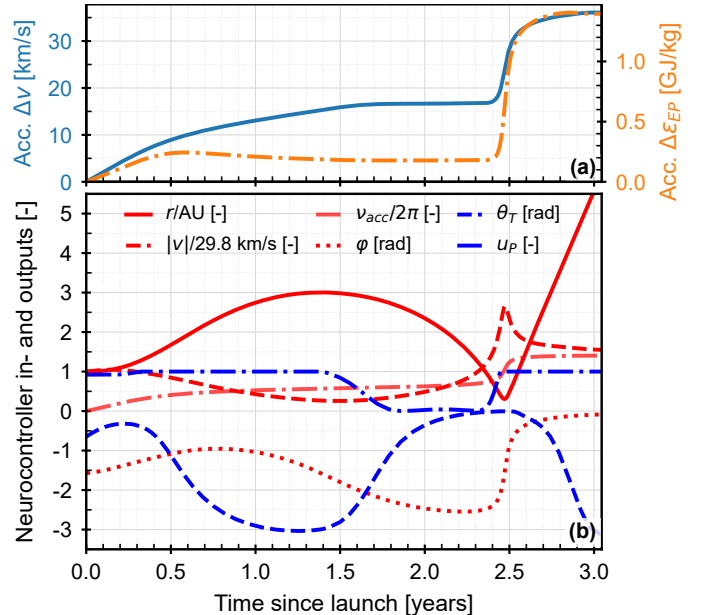


Figure B.10: Learned steering profile for the SOM trajectory without a Jupiter gravity assist. Upper panel: cumulative EP Δv and EP-induced specific orbital energy gain. Lower panel: controller inputs and outputs.

havior. The no-JGA solution keeps $u_P = 1$ directly after perihelion at approximately $t \approx 2.95$ yr, whereas the JGA solution exhibits two minor u_P dips after perihelion. Three explanations are plausible. First, in the JGA case, the SEP–SOM also shapes the subsequent Jupiter approach geometry, which affects the effectiveness of the gravity assist. The energy gain of the JGA depends on the angle of approach [114]. Hence a strictly lo-

cal energy gain right after perihelion due to higher velocity may be traded for a favorable post-SOM velocity vector and encounter geometry. It is noted that in the first dip only u_P deviates slightly from unity, while θ_T remains close to 0 rad. Any significant deviations of θ_T would lead to sub-optimal usage of propellant due to sub-optimal energy gain, as indicated by Eq. (1). Second, since the JGA provides additional Δv , propellant can be saved to increase payload mass, which can manifest as $u_P < 1$. Third, the variation may reflect minor sub-optimality from the evolutionary tuning of ξ .

Appendix C. Supplementary material: Detailed Derivation of the Generalization Equation

Appendix C.1. Setup and first principle

We consider heliocentric motion with thrust:

$$\ddot{\mathbf{r}}(t) = -\frac{GM_{\odot}}{r(t)^3} \mathbf{r}(t) + \frac{F_T(t)}{m(t)} \hat{\mathbf{t}}(t), \quad (\text{C.1})$$

where $m(t)$ is the spacecraft mass, $F_T(t)$ the thrust magnitude, and $\hat{\mathbf{t}}(t)$ the thrust-direction unit vector (parameterized by the thrust angle $\theta_T(t)$). For two designs started from identical initial conditions to follow the *same* trajectory $\mathbf{r}(t)$, the commanded thrust direction and thrust-acceleration history must match pointwise. A convenient statement of this requirement is

$$\hat{\mathbf{t}}(t) \text{ identical}, \quad \frac{F_T(t)}{m(t)} \text{ identical } \forall t. \quad (\text{C.2})$$

Appendix C.2. Power-thrust-mass model

Let the EPS deliver power according to a $1/r^k$ law with throttle $u_P(t) \in [0, 1]$:

$$f(t) \equiv \left(\frac{1 \text{ AU}}{r(t)}\right)^k, \quad P(t) = \alpha_{\text{EPS}} m_{\text{EPS}} f(t) u_P(t), \quad (\text{C.3})$$

where α_{EPS} is the EPS specific power at 1 AU and $m_{\text{EPS}} = \mu_{\text{EPS}} m_0$ is the EPS mass (with m_0 the launch mass). Assuming constant exhaust velocity c_e and thrust efficiency η (taken identical for the compared designs),

$$\begin{aligned} F_T(t) &= \frac{2\eta}{c_e} P(t), \\ \dot{m}(t) &= -\frac{F_T(t)}{c_e} = -\frac{2\eta}{c_e^2} \alpha_{\text{EPS}} m_{\text{EPS}} f(t) u_P(t). \end{aligned} \quad (\text{C.4})$$

Define the throttled-irradiance integral

$$G(t) \equiv \int_0^t f(t') u_P(t') dt'. \quad (\text{C.5})$$

Integrating (C.4) gives

$$m(t) = m_0 - \frac{2\eta}{c_e^2} \alpha_{\text{EPS}} m_{\text{EPS}} G(t), \quad (\text{C.6})$$

and the thrust-acceleration magnitude

$$\frac{F_T(t)}{m(t)} = \frac{\frac{2\eta}{c_e} \alpha_{\text{EPS}} m_{\text{EPS}} f(t) u_P(t)}{m_0 - \frac{2\eta}{c_e^2} \alpha_{\text{EPS}} m_{\text{EPS}} G(t)}. \quad (\text{C.7})$$

Appendix C.3. Trajectory-preserving invariant (allowing variable launch mass)

Consider two designs, “sim” (reference) and “new”, with potentially different launch masses $m_{0,\text{sim}}$ and $m_{0,\text{new}}$, but the same η , c_e , and pointing history $\hat{\mathbf{t}}(t)$. Substituting $m_{\text{EPS}} = \mu_{\text{EPS}} m_0$ into (C.7) yields

$$\frac{F_T(t)}{m(t)} = \frac{\frac{2\eta}{c_e} \alpha_{\text{EPS}} \mu_{\text{EPS}} m_0 f(t) u_P(t)}{m_0 - \frac{2\eta}{c_e^2} \alpha_{\text{EPS}} \mu_{\text{EPS}} m_0 G(t)} = \frac{\frac{2\eta}{c_e} \alpha_{\text{EPS}} \mu_{\text{EPS}} f(t) u_P(t)}{1 - \frac{2\eta}{c_e^2} \alpha_{\text{EPS}} \mu_{\text{EPS}} G(t)}. \quad (\text{C.8})$$

In this reduced form, the explicit factor m_0 cancels; the acceleration history is controlled by $\alpha_{\text{EPS}} \mu_{\text{EPS}}$ together with the throttle history $u_P(t)$ (and the induced history term $G(t)$).

A practical trajectory-preserving condition is the pointwise equality

$$\alpha_{\text{EPS}} \mu_{\text{EPS}} u_P(t) = \alpha_{\text{EPS,sim}} \mu_{\text{EPS,sim}} u_{P,\text{sim}}(t) \quad \forall t, \quad (\text{C.9})$$

which ensures identical thrust-acceleration histories through (C.8) under the stated assumptions.

Two useful corollaries follow:

Appendix C.3.1. (i) Unchanged throttle

If $u_P(t) = u_{P,\text{sim}}(t)$ is retained, then

$$\alpha_{\text{EPS}} \mu_{\text{EPS}} = \alpha_{\text{EPS,sim}} \mu_{\text{EPS,sim}}. \quad (\text{C.10})$$

This expresses a scale-invariant trade between EPS specific power and EPS mass fraction for a fixed throttle schedule.

Appendix C.3.2. (ii) Throttle compensation

If $\alpha_{\text{EPS}} \mu_{\text{EPS}}$ changes, the same trajectory can still be targeted by adjusting the throttle according to

$$u_P(t) = u_{P,\text{sim}}(t) \frac{\alpha_{\text{EPS,sim}} \mu_{\text{EPS,sim}}}{\alpha_{\text{EPS}} \mu_{\text{EPS}}}, \quad 0 \leq u_P(t) \leq 1 \quad \forall t. \quad (\text{C.11})$$

Appendix C.4. Mass budget and payload expression

Let $\mu_p \equiv m_{\text{prop}}(0)/m_0$, $\mu_s \equiv m_s/m_0$, and $\mu_{\text{pl}} \equiv m_{\text{pl}}/m_0$. Under the trajectory-preserving condition (C.9), the normalized mass history implied by (C.6) is the same, and in particular the required propellant mass fraction μ_p is unchanged between the compared cases (for a common terminal time and throttle history). Hence the mass budget in terms of fractions is

$$\mu_{\text{pl}} = (1 - \mu_p) - \mu_s - \mu_{\text{EPS}}. \quad (\text{C.12})$$

Under the unchanged-throttle invariant (C.10), the EPS mass fraction satisfies

$$\mu_{\text{EPS}} = \frac{\alpha_{\text{EPS,sim}} \mu_{\text{EPS,sim}}}{\alpha_{\text{EPS}}}. \quad (\text{C.13})$$

Substituting (C.13) into (C.12) gives

$$\mu_{\text{pl}} = (1 - \mu_p) - \mu_s - \frac{\alpha_{\text{EPS,sim}} \mu_{\text{EPS,sim}}}{\alpha_{\text{EPS}}}. \quad (\text{C.14})$$

Multiplying by the launch mass of the “new” case yields the payload mass:

$$m_{\text{pl,new}} = m_{0,\text{new}} \left[(1 - \mu_p) - \mu_s - \frac{\alpha_{\text{EPS,sim}} \mu_{\text{EPS,sim}}}{\alpha_{\text{EPS}}} \right]. \quad (\text{C.15})$$

Appendix C.4.1. Remarks

- (i) The invariance assumes identical c_e and η , and identical pointing histories $\hat{\mathbf{t}}(t)$.
- (ii) If throttle compensation (C.11) saturates (i.e., $u_P(t) > 1$ at some t), the same trajectory cannot be maintained with that $(\alpha_{EPS}, \mu_{EPS})$ pair under the present model.
- (iii) The exponent κ in $f(t)$ is arbitrary for this derivation; it cancels in the invariance because $f(t)$ is common when $\mathbf{r}(t)$ is identical.

References

- [1] P. C. Brandt, E. Provornikova, A. Cocoros, D. Turner, R. DeMajistre, K. Runyon, C. Lisse, S. Bale, W. Kurth, A. Galli, et al., Interstellar probe: Humanity's exploration of the galaxy begins, *Acta Astronautica* 199 (2022) 364–373. doi:[10.1016/j.actaastro.2022.07.011](https://doi.org/10.1016/j.actaastro.2022.07.011).
- [2] P. Brandt, E. Provornikova, S. D. Bale, A. Cocoros, R. DeMajistre, K. Dialynas, H. A. Elliott, S. Eriksson, B. Fields, A. Galli, et al., Future exploration of the outer heliosphere and very local interstellar medium by interstellar probe, *Space Science Reviews* 219 (2023) 18. doi:[10.1007/s11214-022-00943-x](https://doi.org/10.1007/s11214-022-00943-x).
- [3] J. Linsky, S. Redfield, E. Moebius, What lies outside of the heliopause: Connecting the outer heliosphere with the very local interstellar medium, *Bulletin of the American Astronomical Society* 55 (2023) 190. doi:[10.3847/25c2cfcb.bda427cda](https://doi.org/10.3847/25c2cfcb.bda427cda).
- [4] S. Eriksson, A. Mallet, M. Swisdak, M. Opher, E. Provornikova, S. Bale, M. Desai, A. Alexandrova, Helio2050 white paper: Magnetic reconnection science in the outer heliosphere, *Bulletin of the American Astronomical Society* 55 (2021). doi:[10.3847/25c2cfcb.f5c0635b](https://doi.org/10.3847/25c2cfcb.f5c0635b).
- [5] NASA Office of Inspector General, NASA's Transition of the Space Launch System to a Commercial Services Contract, Technical Report IG-24-001, National Aeronautics and Space Administration, 2023. URL: <https://oig.nasa.gov/wp-content/uploads/2023/10/ig-24-001.pdf>.
- [6] National Aeronautics and Space Administration, Nasa awards launch services contract for goes-u mission, NASA News Release C21-025, 2021. URL: <https://www.nasa.gov/news-release/nasa-awards-launch-services-contract-for-goes-u-mission/>, accessed 2026-01-29.
- [7] R. C. Hopkins, H. D. Thomas, B. M. Wiegmann, A. F. Heaton, L. Johnson, M. F. Baysinger, B. R. Beers, Propulsion Technology Assessment: Science & Enabling Technologies to Explore the Interstellar Medium, NASA Technical Report M15-4779, National Aeronautics and Space Administration, 2015. URL: <https://ntrs.nasa.gov/api/citations/20160004404/downloads/20160004404.pdf>.
- [8] R. P. Rudd, J. C. Hall, G. L. Spradlin, The voyager interstellar mission, *Acta Astronautica* 40 (1997) 383–396. doi:[10.1016/S0094-5765\(97\)00146-X](https://doi.org/10.1016/S0094-5765(97)00146-X).
- [9] J. D. Richardson, L. F. Burlaga, H. Elliott, W. S. Kurth, Y. D. Liu, R. von Steiger, Observations of the outer heliosphere, heliosheath, and interstellar medium, *Space Science Reviews* 218 (2022) 35. doi:[10.1007/s11214-022-00899-y](https://doi.org/10.1007/s11214-022-00899-y).
- [10] S. Fuselier, S. Petrinec, M. Bobra, I. Cairns, Reconnection at the heliopause: Comparing the voyager 1 and 2 heliopause crossings, in: *Journal of Physics: Conference Series*, volume 1620, 2020, p. 012004. doi:[10.1088/1742-6596/1620/1/012004](https://doi.org/10.1088/1742-6596/1620/1/012004).
- [11] M. Haque, M. Shaik Fahad, A. Goyal, B. N. Singh, P. Sahu, B. Neelur, D. K. Punna, L. Dahiya, Voyagers beyond time: The scientific and cultural legacy of nasa's voyager missions in the era of interstellar exploration, *International Journal of Scientific Research & Engineering Trends* 11 (2025). doi:[10.5281/zenodo.17568692](https://doi.org/10.5281/zenodo.17568692).
- [12] J. J. Uri, Voyager's Grand Tour, NASA Technical Report JSC-CN-40453, NASA Johnson Space Center, Houston, TX, United States, 2017. URL: <https://ntrs.nasa.gov/citations/20170009181>, public Use Permitted.
- [13] A. J. Butrica, Voyager: The Grand Tour of Big Science, in: P. E. Mack (Ed.), *From Engineering Science to Big Science: The NACA and NASA Collier Trophy Research Project Winners*, NASA SP-4219, 1998, p. 251. URL: <https://ui.adsabs.harvard.edu/abs/1998fesb.conf..251B>.
- [14] J. J. Benkoski, W. Lloyd Luedeman, N. N. De, M. C. Brupbacher, M. Presley, D. M. Deglau, J. A. Scroggins, W. M. Buchta, D. Zhang, J. D. Mitchell, Combined heat shield and solar thermal propulsion system for an obert maneuver, *Journal of Propulsion and Power* 39 (2023) 284–293. doi:[10.2514/1.B38595](https://doi.org/10.2514/1.B38595).
- [15] A. R. Davoyan, J. N. Munday, N. Tabiryan, G. A. Swartzlander, L. Johnson, Photonic materials for interstellar solar sailing, *Optica* 8 (2021) 722–734. doi:[10.1364/OPTICA.417007](https://doi.org/10.1364/OPTICA.417007).
- [16] S. Mazouffre, Electric propulsion for satellites and spacecraft: established technologies and novel approaches, *Plasma Sources Science and Technology* 25 (2016) 033002. doi:[10.1088/0963-0252/25/3/033002](https://doi.org/10.1088/0963-0252/25/3/033002).
- [17] A. Genovese, N. Maraqtan, Advanced electric propulsion concepts for fast missions to the outer solar system and beyond, *Journal of the British Interplanetary Society (JBIS)* 76 (2023) 114–121. URL: <https://bis-space.com/shop/product/jbis-076-04-0114/>.
- [18] N. Maraqtan, D. Fries, A. Genovese, Advanced electric propulsion systems with optimal specific impulses for fast interstellar precursor missions, in: *Proceedings of the 75th International Astronautical Congress (IAC)*, Milan, Italy, 2024. URL: https://www.researchgate.net/publication/385172298_Advanced_Electric_Propulsion_Systems_with_Optimal_Specific_Impulses_for_Fast_Interstellar_Precursor_Missions, published at the 75th IAC, Milan, Italy, October 14–18, 2024.
- [19] E. A. Bering, A. Parker, M. Giambusso, M. Carter, J. Squire, F. C. Diaz, S. M. Horst, Solar and hybrid electric propulsion to the kuiper belt and beyond, *Bulletin of the American Astronomical Society* 53 (2021) 307. doi:[10.3847/25c2cfcb.72e37e1a](https://doi.org/10.3847/25c2cfcb.72e37e1a).
- [20] A. Ohndorf, B. Dachwald, W. Seboldt, K.-H. Schartner, Flight times to the heliopause using a combination of solar and radioisotope electric propulsion, in: *32nd International Electric Propulsion Conference, IEPC-2011-051*, Wiesbaden, 2011. URL: <https://elib.dlr.de/70898/1/IEPC-2011-051.pdf>.
- [21] E. E. Perl, J. Simon, J. F. Geisz, et al., Development of high-bandgap algainp solar cells grown by organometallic vapor-phase epitaxy, *IEEE Journal of Photovoltaics* 6 (2016) 770–776. doi:[10.1109/JPHOTOV.2016.2537543](https://doi.org/10.1109/JPHOTOV.2016.2537543).
- [22] E. E. Perl, J. Simon, D. J. Friedman, et al., (al)gainp/gaas tandem solar cells for power conversion at elevated temperature and high concentration, *IEEE Journal of Photovoltaics* 8 (2018) 640–645. doi:[10.1109/JPHOTOV.2017.2783853](https://doi.org/10.1109/JPHOTOV.2017.2783853).
- [23] Y. Sun, J. Faucher, D. Jung, M. Vaisman, C. McPheevers, P. Sharps, E. Perl, J. Simon, M. Steiner, D. Friedman, et al., Thermal stability of gaas solar cells for high temperature applications, in: *2016 IEEE 43rd Photovoltaic Specialists Conference (PVSC)*, IEEE, 2016, pp. 2385–2388. doi:[10.1109/PVSC.2016.7750068](https://doi.org/10.1109/PVSC.2016.7750068).
- [24] N. Maraqtan, A. Genovese, W. van Lynden, Streamlined evolutionary neurocontrol for re-evaluation of low thrust solar obert maneuvers to the heliopause, in: *Proceedings of the First European Interstellar Symposium (FEIS)*, Luxembourg, 2024. URL: https://www.researchgate.net/publication/387020767_Streamlined_Evolutionary_Neurocontrol_for_Re-Evaluation_of_Low_Thrust_Solar_Oberth_Maneuvers_to_the_Heliopause.
- [25] H. Oberth, *Wege zur Raumfahrt*, R. Oldenbourg Verlag, München-Berlin, Germany, 1929. URL: https://archive.org/details/nasa_techdoc_19720008133/page/n9/mode/2up, original work in German. English translation available as *Ways to Spaceflight* (NASA TT F-622, 1970).
- [26] R. W. Lyman, M. E. Ewing, R. S. Krishnan, D. M. Lester, J. Ralph L. McNutt, Solar thermal propulsion for an interstellar probe, in: *37th AIAA/ASME/SAE/ASEE Joint Propulsion Conference*, American Institute of Aeronautics and Astronautics (AIAA), Salt Lake City, Utah, USA, 2001. URL: <https://www.kiss.caltech.edu/workshops/ism/presentations/AIAA-2001-3377-169.pdf>. doi:[10.2514/6.2001-3377](https://doi.org/10.2514/6.2001-3377).
- [27] J. Sauder, M. Preudhomme, J. Mueller, D. Cheikh, E. Sunada, R. R.

- Karimi, A. Couto, N. Arora, J. Rapinchuk, L. Alkalai, System engineering a solar thermal propulsion mission concept for rapid interstellar medium access, *Advances in Astronautics Science and Technology* 4 (2021) 77–90. doi:[10.1007/s42423-021-00077-2](https://doi.org/10.1007/s42423-021-00077-2).
- [28] A. Hibberd, A. M. Hein, Project lyra: catching 1i/'oumuamua—using nuclear thermal rockets, *Acta Astronautica* 179 (2021) 594–603. doi:[10.1016/j.actaastro.2020.11.038](https://doi.org/10.1016/j.actaastro.2020.11.038).
- [29] A. Hibberd, M. Lingam, A. M. Hein, Can we fly to planet 9?, arXiv preprint arXiv:2208.10207 (2022). URL: <https://arxiv.org/abs/2208.10207>.
- [30] C. A. Bailer-Jones, The sun diver: Combining solar sails with the obert effect, *American Journal of Physics* 89 (2021) 235–243. doi:[10.1119/10.0002178](https://doi.org/10.1119/10.0002178).
- [31] A. Davoyan, H. Helvajian, L. Johnson, M. Velli, Extreme Metamaterial Solar Sails for Breakthrough Space Exploration: NIAC Phase II Final Report, Contractor or Grantee Report NASA/NIAC Final Report, NASA Innovative Advanced Concepts (NIAC), Washington, DC, 2024. URL: <https://ntrs.nasa.gov/citations/20250008150>. doi:[20250008150](https://doi.org/10.20250008150), contract/Grant: 80NSSC21K0954. Distribution: Public. Use by or on behalf of the U.S. Government permitted.
- [32] C. A. Kluever, Trajectory Optimization of an Interstellar Mission Using Solar Electric Propulsion, NASA Contractor Report NASA/CR-97-206527, NASA Lewis Research Center, Cleveland, OH, 1997. URL: <https://ntrs.nasa.gov/citations/19980004505>, final Report for NASA grant NAG3-1731.
- [33] H. W. Loeb, K.-H. Schartner, B. Dachwald, A. Ohndorf, W. Seboldt, An interstellar–heliosopause mission using a combination of solar/radioisotope electric propulsion, in: 32nd International Electric Propulsion Conference, IEPC-2011-052, Wiesbaden, 2011. URL: <https://electricrocket.org/IEPC/IEPC-2011-052.pdf>.
- [34] A. Hibberd, T. M. Eubanks, Catching 3i/atlas using a solar obert, 2026. URL: <https://arxiv.org/abs/2601.02533>. arXiv:2601.02533.
- [35] P. C. Liewer, R. A. Mewaldt, J. A. Ayon, R. A. Wallace, Nasa's interstellar probe mission, in: M. S. El-Genk (Ed.), Space Technology and Applications International Forum–2000, volume 504 of *AIP Conference Proceedings*, American Institute of Physics, Melville, NY, 2000, pp. 911–916. URL: https://www.researchgate.net/profile/Richard-Mewaldt/publication/254001285_NASA%27s_interstellar_probe_mission/links/56f0280c08ae584badc92c5f/NASAs-interstellar-probe-mission.pdf. doi:[10.1063/1.1302594](https://doi.org/10.1063/1.1302594).
- [36] A. Hibberd, A. M. Hein, Project lyra: Catching 1i/'oumuamua – using laser sailcraft in 2030, 2020. URL: <https://arxiv.org/abs/2006.03891>. doi:[10.1016/j.actaastro.2020.11.038](https://doi.org/10.1016/j.actaastro.2020.11.038). arXiv:2006.03891.
- [37] J. M. Shoji, P. E. Frye, J. A. McClanahan, Solar thermal propulsion status and future, in: AIAA Space Programs and Technologies Conference (AIAA Space Forum), American Institute of Aeronautics and Astronautics (AIAA), Huntsville, AL, USA, 1992. doi:[10.2514/6.1992-1719](https://doi.org/10.2514/6.1992-1719).
- [38] A. Irvine, R. Hetterich, S. J. Edwards, M. A. Rodriguez, Design reference mission development for nuclear thermal propulsion enabled science missions, in: ASCEND 2020, 2020, p. 4126. URL: https://ntrs.nasa.gov/api/citations/20205007947/downloads/NTP_for_Science_STRIVES_submission.pdf.
- [39] C. L. Zola, Interplanetary Probe Missions with Solar-Electric Propulsion Systems, NASA Technical Note NASA-TN-D-5293, National Aeronautics and Space Administration, Lewis Research Center, 1969. URL: <https://ntrs.nasa.gov/api/citations/19690020360/downloads/19690020360.pdf>.
- [40] D. H. Rodgers, J. R. Brophy, Ion propulsion technology for fast missions to pluto, in: Proceedings of the International Electric Propulsion Conference (IEPC), IEPC-01-179, Pasadena, 2001. URL: https://electricrocket.org/IEPC/176_1.pdf.
- [41] A. V. Ilin, L. D. Cassady, T. W. Glover, M. D. Carter, F. R. Chang Díaz, A Survey of Missions using VASIMR for Flexible Space Exploration, Technical Report JSC-65825, Ad Astra Rocket Company (prepared for NASA under PO NNNJ10HB38P), 2010. URL: https://www.adastrarocket.com/technical-papers-archives/VASIMR_for_flexible_space_exploration.pdf.
- [42] O. Dupré, R. Vaillon, M. A. Green, Thermal behavior of photovoltaic devices, *Physics and engineering* 10 (2017) 978–3. URL: <https://link.springer.com/book/10.1007/978-3-319-49457-9>. doi:[10.1007/978-3-319-49457-9](https://doi.org/10.1007/978-3-319-49457-9).
- [43] H. Porsche, Helios mission: Mission objectives, mission verification, selected results, in: Solar system and its exploration, ESA SP-164, 1981. URL: <https://ui.adsabs.harvard.edu/abs/1981ESASP.164...43P>.
- [44] G. Landis, J. Kinnison, M. Fraeman, L. Roufberg, S. Vernon, M. Wirzburger, P. Schmitz, Solar power system design for the solar probe+ mission, in: 6th International Energy Conversion Engineering Conference (IECEC), 2008, p. 5712. URL: <https://ntrs.nasa.gov/api/citations/20090004577/downloads/20090004577.pdf>. doi:[10.2514/6.2008-5712](https://doi.org/10.2514/6.2008-5712).
- [45] N. E. Raouafi, L. Matteini, J. Squire, S. Badman, M. Velli, K. Klein, C. Chen, W. Matthaeus, A. Szabo, M. Linton, et al., Parker solar probe: Four years of discoveries at solar cycle minimum, *Space Science Reviews* 219 (2023) 8. URL: <https://link.springer.com/article/10.1007/s11214-023-00952-4>. doi:[10.1007/s11214-023-00952-4](https://doi.org/10.1007/s11214-023-00952-4).
- [46] A. Lyngvi, N. Rando, L. Gerlach, A. Peacock, The solar orbiter thermal design, in: 56th International Astronautical Congress of the International Astronautical Federation, the International Academy of Astronautics, and the International Institute of Space Law, IAC-05-C2.6.01, Fukuoka, 2005. URL: <https://sci.esa.int/s/8dK779W>.
- [47] C. Oberhüttinger, H. Nesswetter, D. Quabis, C. Zimmermann, Simulating large area, high intensity am0 illumination—test results from bepicolombo and solar orbiter qualification, in: E3S Web of Conferences, volume 16, EDP Sciences, 2017, p. 02007. doi:[10.1051/e3sconf/20171602007](https://doi.org/10.1051/e3sconf/20171602007).
- [48] C. G. Marirrodriga, A. Pacros, S. Strandmoe, M. Arcioni, A. Arts, C. Ashcroft, L. Ayache, Y. Bonnefous, N. Brahimi, F. Cipriani, et al., Solar orbiter: Mission and spacecraft design, *Astronomy & Astrophysics* 646 (2021) A121. doi:[10.1051/0004-6361/202038519](https://doi.org/10.1051/0004-6361/202038519).
- [49] D. A. Scheiman, G. A. Landis, V. G. Weizer, High-bandgap solar cells for near-sun missions, in: AIP Conference Proceedings, volume 458, American Institute of Physics, 1999, pp. 616–620. doi:[10.1063/1.57701](https://doi.org/10.1063/1.57701).
- [50] M. Spitzer, J. Dingle, R. Gale, P. Zavracky, M. Boden, D. Doyle, Gallium arsenide concentrator solar cells with highly stable metallization, in: Conference Record of the Twentieth IEEE Photovoltaic Specialists Conference, 1988, pp. 930–933 vol.2. doi:[10.1109/PVSC.1988.105840](https://doi.org/10.1109/PVSC.1988.105840).
- [51] S. Bailey, R. Raffaelle, Silicon Carbide Solar Cells Investigated, NASA Technical Memorandum 2002-211614, NASA Glenn Research Center, 2001. URL: <https://ntrs.nasa.gov/api/citations/20050201668/downloads/20050201668.pdf>, accessed: 2025-10-16.
- [52] K. Nishioka, T. Takamoto, T. Agui, M. Kaneiwa, Y. Uraoka, T. Fuyuki, Evaluation of temperature characteristics of high-efficiency ingap/ingaas/ge triple-junction solar cells under concentration, *Solar energy materials and solar cells* 85 (2005) 429–436. doi:[10.1016/j.solmat.2004.05.008](https://doi.org/10.1016/j.solmat.2004.05.008).
- [53] C. Brandt, C. Baur, A. Caon, P. Müller-Buschbaum, C. Zimmermann, T. Andreev, The influence of high temperatures on radiation damage of gainp 2/gaas/ge triple junction cells, in: 2012 IEEE 38th Photovoltaic Specialists Conference, PVSC 2012, number PART 2 in Conference Record of the IEEE Photovoltaic Specialists Conference, 2012. doi:[10.1109/PVSC-Vol2.2012.6656726](https://doi.org/10.1109/PVSC-Vol2.2012.6656726), 2012 IEEE 38th Photovoltaic Specialists Conference, PVSC 2012 ; Conference date: 03-06-2012 Through 08-06-2012.
- [54] E. E. Perl, J. Simon, J. F. Geisz, M. L. Lee, D. J. Friedman, M. A. Steiner, Measurements and modeling of iii-v solar cells at high temperatures up to 400 °c, *IEEE Journal of Photovoltaics* 6 (2016) 1345–1352. doi:[10.1109/JPHOTOV.2016.2582398](https://doi.org/10.1109/JPHOTOV.2016.2582398).
- [55] J. Grandidier, A. P. Kirk, P. Jahelka, M. A. Stevens, P. K. Gogna, D. Crisp, M. L. Osowski, T. E. Vandervelde, H. A. Atwater, J. A. Cutts, Photovoltaic operation in the lower atmosphere and at the surface of venus, *Progress in Photovoltaics: Research and Applications* 28 (2020) 545–553. doi:[10.1002/pip.3214](https://doi.org/10.1002/pip.3214).
- [56] Y. Zhao, M. Xu, X. Huang, J. Lebeau, T. Li, D. Wang, H. Fu, K. Fu, X. Wang, J. Lin, H. Jiang, Toward high efficiency at high tempera-

- tures: Recent progress and prospects on ingan-based solar cells, *Materials Today Energy* 31 (2022) 101229. doi:[10.1016/j.mtener.2022.101229](https://doi.org/10.1016/j.mtener.2022.101229).
- [57] D. Petry, C. Grunwald, A. Lohberg, A. Brandi, C. Oxynos-Lauschke, T. Andreev, R. Van Der Ven, U. Schuhmacher, S. Fugger, A. Caon, H. K. Fiebrich, The Bepi Colombo Mercury Transfer Module And Mercury Planetary Orbiter Solar Array Design And Development, in: 9th European Space Power Conference, volume 690 of *ESA Special Publication*, 2011, p. 98. URL: <https://ui.adsabs.harvard.edu/abs/2011ESASP.690E..98P>.
- [58] A. Boca, P. Blumenfeld, K. Crist, K. De Zetter, B. Richards, C. Sarver, P. Sharps, R. Stall, M. Stan, Uv-exposure experiments for the solar probe plus array, in: 2013 IEEE 39th Photovoltaic Specialists Conference (PVSC), 2013, pp. 3115–3120. doi:[10.1109/PVSC.2013.6745119](https://doi.org/10.1109/PVSC.2013.6745119).
- [59] A. Lindner, C. Oberhütziner, C. Paarmann, J. Müller, S. Strandmoe, I. Costello, Solar orbiter solar array-exceptional design for a hot mission, in: 2019 European Space Power Conference (ESPC), IEEE, 2019, pp. 1–7. doi:[10.1109/ESPC.2019.8932039](https://doi.org/10.1109/ESPC.2019.8932039).
- [60] N. S. Fatemi, H. E. Pollard, H. Q. Hou, P. R. Sharps, Solar array trades between very high-efficiency multi-junction and si space solar cells, in: Conference Record of the Twenty-Eighth IEEE Photovoltaic Specialists Conference-2000 (Cat. No. 00CH37036), IEEE, 2000, pp. 1083–1086. doi:[10.1109/PVSC.2000.916075](https://doi.org/10.1109/PVSC.2000.916075).
- [61] M. A. Mejía Escobar, C. Algara, Surveying the potential of flexible and high-specific-power photovoltaic assemblies and arrays for space applications, *Joule* 9 (2025) 102194. doi:[10.1016/j.joule.2025.102194](https://doi.org/10.1016/j.joule.2025.102194).
- [62] K. Nassiri Nazif, A. Daus, J. Hong, N. Lee, S. Vaziri, A. Kumar, F. Nitta, M. E. Chen, S. Kananian, R. Islam, et al., High-specific-power flexible hopkins metal dichalcogenide solar cells, *Nature Communications* 12 (2021) 7034. doi:[10.1038/s41467-021-27195-7](https://doi.org/10.1038/s41467-021-27195-7).
- [63] A. W. Ho-Baillie, H. G. Sullivan, T. A. Bannerman, H. P. Talathi, J. Bing, S. Tang, A. Xu, D. Bhattacharyya, I. H. Cairns, D. R. McKenzie, Deployment opportunities for space photovoltaics and the prospects for perovskite solar cells, *Advanced Materials Technologies* 7 (2022) 2101059. doi:[10.1002/admt.202270010](https://doi.org/10.1002/admt.202270010).
- [64] Y. Tu, J. Wu, G. Xu, X. Yang, R. Cai, Q. Gong, R. Zhu, W. Huang, Perovskite solar cells for space applications: progress and challenges, *Advanced Materials* 33 (2021) 2006545. doi:[10.1002/adma.202006545](https://doi.org/10.1002/adma.202006545).
- [65] M. Kaltenbrunner, G. Adam, E. D. Glowacki, M. Drack, R. Schwödiauer, L. Leonat, D. H. Apaydin, H. Groiss, M. C. Scharber, M. S. White, et al., Flexible high power-per-weight perovskite solar cells with chromium oxide-metal contacts for improved stability in air, *Nature Materials* 14 (2015) 1032–1039. doi:[10.1038/nmat4388](https://doi.org/10.1038/nmat4388).
- [66] S. Kang, J. Jeong, S. Cho, Y. J. Yoon, S. Park, S. Lim, J. Y. Kim, H. Ko, Ultrathin, lightweight and flexible perovskite solar cells with an excellent power-per-weight performance, *J. Mater. Chem. A* 7 (2019) 1107–1114. URL: <http://dx.doi.org/10.1039/C8TA10585E>. doi:[10.1039/C8TA10585E](https://doi.org/10.1039/C8TA10585E).
- [67] J. Jackson, M. Allen, R. Myers, E. Soendker, B. Welander, A. Tolentino, S. Hablitzel, C. Yeatts, S. Xu, C. Sheehan, J. Cardin, J. S. Snyder, R. R. Hofer, T. Tofil, D. Herman, 13kW Advanced Electric Propulsion Flight System Development and Qualification, in: Proceedings of the 35th International Electric Propulsion Conference (IEPC 2017), Electric Rocket Propulsion Society, Atlanta, Georgia, USA, 2017. URL: https://electricrocket.org/IEPC/IEPC_2017_223.pdf, paper IEPC-2017-223, October 8–12, 2017.
- [68] R. Fockema, High Efficiency Solar Arrays – Executive Summary Report, Executive Summary Report HESA-ESR-ADSN-SA-001, Airbus Netherlands B.V. (Airbus NL), 2023. URL: https://nebula.esa.int/sites/default/files/neb_tec_study/2428/public/HESA-ESR-ADSN-SA-001%20HESA%20Executive%20Summary%20Report.pdf, eSA Contract No. 4000131244/20/NL/FE; available via ESA Nebula Public Library.
- [69] National Aeronautics and Space Administration, MegaFlex solar array scale-up, up to 175 kw per wing, NASA TechPort project database 9879, 2025. URL: <https://techport.nasa.gov/projects/9879>, lead organization: Angstrom Designs, Inc.; page updated 18 Dec 2025.
- [70] D. R. Jovel, M. L. R. Walker, D. A. Herman, Review of High-Power Electrostatic and Electrothermal Electric Propulsion, *Journal of Propulsion and Power* 38 (2022) 1051–1081. URL: https://hpepl.ae.gatech.edu/sites/default/files/files/Review%20of%20HP%20ES%20ET%20EP_JPP%20Nov%202022.pdf. doi:[10.2514/1.B38594](https://doi.org/10.2514/1.B38594).
- [71] L. R. Piñero, K. E. Bozak, W. Santiago, R. J. Scheidegger, A. G. Birchenough, Development of high-power hall thruster power processing units at nasa grc, in: AIAA/SAE/ASEE Joint Propulsion Conference, Orlando, FL, USA, 2015. URL: <https://ntrs.nasa.gov/citations/20150023095>, nASA NTRS Document ID: 20150023095; Report No. GRC-E-DAA-TN24681.
- [72] B. Reese, Silicon carbide (sic) power processing unit (ppu) for hall effect thrusters, NASA Technical Reports Server (NTRS); publication in *An Overview of SBIR Phase 2 In-Space Propulsion and Cryogenic Fluids Management*, 2015. URL: <https://ntrs.nasa.gov/citations/20160005345>, nASA NTRS Document ID: 20160005345.
- [73] J. E. Polk, D. M. Goebel, J. S. Snyder, A. C. Schneider, L. K. Johnson, A. Sengupta, A high power ion thruster for deep space missions, *Review of Scientific Instruments* 83 (2012). doi:[10.1063/1.4728415](https://doi.org/10.1063/1.4728415).
- [74] J. P. Luna, R. Lewis, N. Park, J. Bosher, F. Guarducci, F. Cannat, T7 thruster design and performance, in: Proceedings of the 36th International Electric Propulsion Conference, Wien, Austria, IEPC-2019-356, Vienna, 2019, pp. 15–20. URL: <https://electricrocket.org/2019/356.pdf>.
- [75] H. J. Leiter, R. Kukies, J.-P. Porst, J. Kuhmann, M. Berger, M. Rath, Results from the rit-22 technology maturity demonstration activity, in: 50th AIAA/ASME/SAE/ASEE Joint Propulsion Conference, AIAA 2014-3421, Cleveland, 2014. doi:[10.2514/6.2014-3421](https://doi.org/10.2514/6.2014-3421).
- [76] A. Boxberger, G. Herdrich, Integral measurements of 100 kw class steady state applied-field magnetoplasmadynamic thruster sx3 and perspectives of af-mdp technology, in: 35th International Electric Propulsion Conference, IEPC-2017-339, Atlanta, GA, 2017, pp. 8–12. URL: https://electricrocket.org/IEPC/IEPC_2017_339.pdf.
- [77] J. Zheng, H. Liu, Y. Song, C. Zhou, Y. Li, M. Li, H. Tang, G. Wang, Y. Cong, B. Wang, et al., Integrated study on the comprehensive magnetic-field configuration performance in the 150 kw superconducting magnetoplasmadynamic thruster, *Scientific Reports* 11 (2021) 20706. doi:<https://doi.org/10.1038/s41598-021-01675-8>.
- [78] M. LaPointe, E. Strzempkowski, E. Pencil, High power MPD thruster performance measurements, in: 40th AIAA/ASME/SAE/ASEE Joint Propulsion Conference and Exhibit, AIAA-2004-3467, TM-2004-213226, 2004, p. 3467. URL: <https://ntrs.nasa.gov/citations/20040139544>.
- [79] J. Monheiser, K. Goodfellow, C. Aubuchon, J. Wang, B. Ferriauolo, G. Williams, G. Soulas, R. Shastry, N. Arthur, A summary of the next-c flight thruster proto-flight testing, in: AIAA Propulsion and Energy Forum, 2021. URL: <https://ntrs.nasa.gov/api/citations/20210018563/downloads/NEXT-C%20AIAA%20Paper%202021%20FINAL.pdf>. doi:[10.2514/6.2021-3408](https://doi.org/10.2514/6.2021-3408).
- [80] D. Goebel, J. Polk, A. Sengupta, Discharge chamber performance of the nexion ion thruster, in: 40th AIAA/ASME/SAE/ASEE Joint Propulsion Conference and Exhibit, AIAA-2004-3813, 2004, p. 3813. URL: https://www.researchgate.net/profile/Jay-Polk/publication/237750382_Discharge_Chamber_Performance_of_the_NEXIS_Ion_Thruster/links/02e7e52b17fac8630e000000/Discharge-Chamber-Performance-of-the-NEXIS-Ion-Thruster.pdf. doi:[10.2514/6.2004-3813](https://doi.org/10.2514/6.2004-3813).
- [81] T. Randolph, J. Polk, An overview of the nuclear electric xenon ion system (nexis) activity, in: 40th AIAA/ASME/SAE/ASEE Joint Propulsion Conference and Exhibit, AIAA-2004-3450, 2004. doi:[10.2514/6.2004-3450](https://doi.org/10.2514/6.2004-3450).
- [82] J. Foster, T. Haag, H. Kamhawi, M. Patterson, S. Malone, F. Elliott, The High Power Electric Propulsion (HiPEP) Ion Thruster, in: 40th AIAA/ASME/SAE/ASEE Joint Propulsion Conference and Exhibit, AIAA-2004-3812, 2004. URL: <https://www.researchgate.net/publication/24298640>. doi:[10.2514/6.2004-3812](https://doi.org/10.2514/6.2004-3812).
- [83] M. S. Konstantinov, V. G. Petukhov, H. W. Loeb, Application of rit-22 thruster for interhelioprobe mission, Moscow Aviation Institute, No. 60 (2012). URL: <https://mai.ru/upload/iblock/d34/application-of-rit-22-thruster-for-interhelioprobe-mission.pdf>.

- [84] R. Killinger, H. Leiter, RITA-An Ion Thruster System for Commercial and Scientific Applications, in: 41st AIAA/ASME/SAE/ASEE Joint Propulsion Conference & Exhibit, AIAA-2005-3886, 2005. doi:[10.2514/6.2005-3886](https://doi.org/10.2514/6.2005-3886).
- [85] M. Han, H. Rana, Applied-field magnetoplasmadynamic thrusters for deep space exploration, 2024. URL: <https://arxiv.org/abs/2410.17478>. arXiv:2410.17478.
- [86] E. Choueiri, Scaling of thrust in self-field magnetoplasmadynamic thrusters, Journal of Propulsion and Power 14 (1998) 744–753. URL: <https://www.researchgate.net/profile/Edgar-Choueiri/publication/245434610>. doi:[10.2514/2.5337](https://doi.org/10.2514/2.5337).
- [87] E. Choueiri, J. Ziemer, Quasi-steady magnetoplasmadynamic thruster measured performance database, in: 34th AIAA/ASME/SAE/ASEE Joint Propulsion Conference and Exhibit, AIAA-98-3472, 1998. URL: <https://eppdylab.cpaneldev.princeton.edu/publications/pdf/choueiri-jpc-1998-3472.pdf>. doi:[10.2514/6.1998-3472](https://doi.org/10.2514/6.1998-3472).
- [88] H. Yao, W. Yang, T. Zhang, B. Wang, H. Tang, Electromagnetic properties analysis on superconducting magnet coil for magnetoplasmadynamic thrusters, Chinese Space Science and Technology 37 (2017) 1–8.
- [89] A. Boxberger, A. Behnke, G. Herdrich, Current advances in optimization of operative regimes of steady state applied field mpd thrusters, in: 36th International Electric Propulsion Conference, IEPC-2019-585, Vienna, 2019. URL: <https://electricrocket.org/2019/585.pdf>.
- [90] C. Zhou, P. Wu, Y.-T. Song, J.-X. Zheng, Y. Li, G. Wang, H.-Y. Liu, Experimental study on performance of 100-kw low temperature superconducting steady-state magnetoplasmadynamic thruster, Chinese Physics B 34 (2025) 025201. doi:[10.1088/1674-1056/ad9910](https://doi.org/10.1088/1674-1056/ad9910).
- [91] R. L. McNutt Jr., R. F. Wimmer-Schweingruber, M. Gruntman, S. M. Krimigis, E. C. Roelof, P. C. Brandt, S. R. Vernon, M. V. Paul, R. W. Stough, J. D. Kinnison, Interstellar probe - Destination: Universe!, Acta Astronautica 196 (2022) 13–28. doi:[10.1016/j.actaastro.2022.04.001](https://doi.org/10.1016/j.actaastro.2022.04.001).
- [92] B. Dachwald, A. Ohndorf, Global Optimization of Continuous-Thrust Trajectories Using Evolutionary Neurocontrol, Springer International Publishing, Cham, 2019, pp. 33–57. doi:[10.1007/978-3-030-10501-3_2](https://doi.org/10.1007/978-3-030-10501-3_2).
- [93] A. Ohndorf, Multiphase low-thrust trajectory optimization using evolutionary neurocontrol, Ph.D. thesis, Delft University of Technology, 2016. doi:[10.4233/uuid:b3d888aa-0a97-4c5e-83c5-23504656f893](https://doi.org/10.4233/uuid:b3d888aa-0a97-4c5e-83c5-23504656f893).
- [94] B. Dachwald, Optimization of very-low-thrust trajectories using evolutionary neurocontrol, Acta Astronautica 57 (2005) 175–185. doi:[10.1016/j.actaastro.2005.03.004](https://doi.org/10.1016/j.actaastro.2005.03.004).
- [95] B. Dachwald, Evolutionary neurocontrol: a smart method for global optimization of low-thrust trajectories, in: AIAA/AAS Astrodynamics Specialist Conference and Exhibit, AIAA-2004-5405, 2004. URL: <https://www.researchgate.net/profile/Bernd-Dachwald/publication/224787115>. doi:[10.2514/6.2004-5405](https://doi.org/10.2514/6.2004-5405).
- [96] G. A. Landis, Solar power for near-sun, high-temperature missions, in: 2008 33rd IEEE Photovoltaic Specialists Conference, IEEE, 2008, pp. 1–5. doi:[10.1109/PVSC.2008.4922857](https://doi.org/10.1109/PVSC.2008.4922857).
- [97] P. Fortescue, G. Swinerd, J. Stark, Spacecraft systems engineering, 4th ed., John Wiley & Sons, 2011. URL: <https://www.wiley.com/en-us/Spacecraft+Systems+Engineering%2C+4th+Edition-p-9780470750124>.
- [98] J. R. Wertz, D. F. Everett, J. J. Puschell (Eds.), Space Mission Engineering: The New SMAD, volume 28 of *Space Technology Library*, Microcosm Press, Hawthorne, CA, USA, 2011. URL: <https://microcosmpress.com/publishing/space-mission-engineering-the-new-smad/>.
- [99] The Johns Hopkins University Applied Physics Laboratory, MESSENGER launch press kit, Press kit (PDF), 2004. URL: https://www.jhuapl.edu/sites/default/files/2023-03/MESSENGER_Launch_Press_Kit.pdf, accessed 2026-01-22.
- [100] NASA, Expendable launch vehicle (elv) performance website, 2025. URL: <https://elvperf.ksc.nasa.gov/Pages/Default.aspx>, accessed: 2025-01-08.
- [101] SpaceX, Falcon heavy, 2025. URL: <https://www.spacex.com/vehicles/falcon-heavy>, accessed: 2025-12-20.
- [102] G. A. Landis, Chapter fourteen - space photovoltaics for extreme high-temperature missions, in: Photovoltaics for Space, Elsevier, 2023, pp. 393–410. doi:[10.1016/B978-0-12-823300-9.00012-1](https://doi.org/10.1016/B978-0-12-823300-9.00012-1).
- [103] G. A. Landis, Power systems for venus surface missions: A review, Acta Astronautica 187 (2020) 424–431. doi:[10.1016/j.actaastro.2020.09.030](https://doi.org/10.1016/j.actaastro.2020.09.030).
- [104] G. B. N. Y. N. A. D. C. G. D. C. C. R. Verduci, V. Romano, Solar energy in space applications: Review and technology perspectives, Advanced Energy Materials 12 (2022) 2200125. doi:[10.1002/aenm.202200125](https://doi.org/10.1002/aenm.202200125).
- [105] J. Li, A. Aierken, Y. Liu, Y. Zhuang, X. Yang, J. Mo, R. Fan, Q. Chen, S. Zhang, Y. Huang, et al., A brief review of high efficiency iii-v solar cells for space application, Frontiers in Physics 8 (2021) 631925. doi:[10.3389/fphy.2020.631925](https://doi.org/10.3389/fphy.2020.631925).
- [106] R. L. McNutt Jr., Nuclear electric propulsion for fast interstellar precursor missions: Physical limits on performance, in: Proceedings of the 76th International Astronautical Congress (IAC), Sydney, Australia, 2025. URL: <https://iafastro.directory/iac/paper/id/96464/summary/>, paper code: IAC-25,D4,4,1,x96464; Session D4.4.
- [107] M. Duchek, A. D. Boylston, D. P. Langford, S. J. Greenhalge, K. A. Polzin, R. M. Myers, Nuclear Electric Propulsion for Science Missions, Technical Report IEPC-2024-721, NASA Glenn Research Center, Toulouse, 2024. URL: https://ntrs.nasa.gov/api/citations/20240007470/downloads/NEPforScienceMissions_IEPC-2024-721_Final.pdf.
- [108] G. Woodcock, L. Kos, L. Johnson, J. Jones, A. Trausch, B. Eberle, H. J. Brady, Benefits of nuclear electric propulsion for outer planet exploration, in: 38th AIAA/ASME/SAE/ASEE Joint Propulsion Conference & Exhibit, AIAA Paper 2002-3548, 2002. URL: <https://ntrs.nasa.gov/api/citations/20020084995/downloads/20020084995.pdf>. doi:[10.2514/6.2002-3548](https://doi.org/10.2514/6.2002-3548).
- [109] A. P. Girija, Aerocapture enabled fast uranus orbiter missions, arXiv preprint arXiv:2310.14514 (2023). doi:[10.48550/arXiv.2310.14514](https://doi.org/10.48550/arXiv.2310.14514).
- [110] L. Johnson, N. Barnes, M. Ceriotti, T. Y. Chen, A. Davoyan, L. Friedman, D. Garber, R. Kezerashvili, K. Kobayashi, G. Matloff, C. McInnes, P. Mulligan, G. Swartzlander, S. G. Turyshev, Solar sail propulsion by 2050: An enabling capability for heliophysics missions, 2023. URL: <https://arxiv.org/abs/2301.01297>. arXiv:2301.01297.
- [111] J. J. Benkoski, Phase I Final Report: Combined Heat Shield and Solar Thermal Propulsion System for an Oberth Maneuver, Final Report 21-NIAC22B-0053, NASA Institute for Advanced Concepts, 2023. URL: <https://ntrs.nasa.gov/citations/20250001946>.
- [112] U. Walter, Astronautics: The Physics of Space Flight, 3rd ed., Springer, 2019. doi:[10.1007/978-3-319-74373-8](https://doi.org/10.1007/978-3-319-74373-8).
- [113] K. E. Tsiolkovsky, The Exploration of Cosmic Space by Means of Reaction Devices, 1903. URL: https://archive.org/details/issledovaniye_mirovykh_prostranstv_reaktivnymi_priborami, original work in Russian. A later reprint (1914) is available at https://archive.org/details/issledovaniye_mirovykh_prostranstv_reaktivnymi_priborami.
- [114] E. Messerschmid, S. Fasoulas, Raumfahrtssysteme: Eine Einführung mit Übungen und Lösungen, Springer Vieweg, Berlin, Heidelberg, 2017. URL: <https://link.springer.com/book/10.1007/978-3-662-49638-1>. doi:[10.1007/978-3-662-49638-1](https://doi.org/10.1007/978-3-662-49638-1).